



LIBRARY
Michigan State
University

ABSTRACT

FAILURE MODES IN CLAY

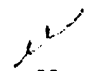
By David L. Warder

An experimental study was made to evaluate the deformation conditions that accompany failure in a clay under axial compression. The type of end restraint and the strain rate were varied in a series of unconfined compression and CFS tests in order to study their effect on the type of failure and on the strength of the clay.

It was found that after the appearance of a single failure surface, further deformation is limited to rigid body sliding along the failure surface. The use of frictionless end plates and shorter samples tend to prevent the formation of a single failure surface and produce multiple slip lines. Frictionless end plates and increased strain rate increase the strength as well as the failure strain.

FAILURE MODES IN CLAY

By


David L. Warder

A THESIS

Submitted to
Michigan State University
in partial fulfillment of the requirements
for the degree of

MASTER OF SCIENCE

Department of Civil Engineering

1964

ACKNOWLEDGMENTS

The writer wishes to express his sincere appreciation to Dr. T. H. Wu, Department of Civil Engineering, under whose supervision this research was carried out. His guidance and encouragement in the preparation of this thesis, as well as throughout the writer's Master's Degree program, have been invaluable. The writer is also indebted to Dr. A. K. Loh for his assistance in the laboratory and for his many worthwhile suggestions.

The writer wishes to thank the National Science Foundation and the Division of Engineering Research at Michigan State University for the Graduate Research Assistantship that made this research possible.

TABLE OF CONTENTS

Chapter	Page
I. INTRODUCTION	1
II. THEORETICAL CONSIDERATIONS	3
2.1 Failure surface	3
2.2 Plasticity solutions for axial symmetry	4
2.3 Solution for axial symmetry by kinematics	7
III. EXPERIMENTAL PROGRAM	10
3.1 Soils used	10
3.2 Preparation of samples	11
3.3 Unconfined compression tests	11
3.4 CFS tests	15
IV. PRESENTATION AND DISCUSSION OF RESULTS . . .	21
4.1 Failure types	21
4.2 Effect on strength	25
V. CONCLUSIONS	32
BIBLIOGRAPHY	34
APPENDICES	35

LIST OF TABLES

Table	Page
1. Index properties	10
2. Final water content variation for consolidated samples	12
3. Summary of testing program on kaolinite	15
4. Summary of unconfined testing program on Sault clay	16
5. Summary of CFS tests	20
6. Results of unconfined compression tests on kaolinite	28
7. Results of unconfined compression tests on Sault clay	29
8. Summary of CFS results	30
9. Summary of CFS results on ϕ_e and C_e	31
10. Data sheet for W-K-U-1	36
11. Data sheet for W-K-U-6	37
12. Data sheet for W-S-U-4	38
13. Data sheet for W-C-CU-2	40
14. General data sheet for WF-CFS-6	49
15. Consolidation data sheet for WF-CFS-6	50
16. Typical CFS data sheet from WF-CFS-6	51
17. CFS calculation sheet for WF-CFS-6	52
18. General data sheet for GF-CFS-2	54
19. Consolidation data sheet for GF-CFS-2	55
20. Typical CFS data sheet from GF-CFS-2	56
21. CFS calculation sheet for GF-CFS-2	57

LIST OF FIGURES

Figure	Page
1. Mohr circle	3
2. Formation of dead zones	4
3. Sketch of deforming region for Eq. (6)	6
4. Sketch of deforming region for Eq. (8)	6
5. Sketch of deforming region for Eq. (13)	9
6. Cross section of frictionless end plates	14
7. Set-up for instantaneous load application	14
8. Sketch of bottom of triaxial sample	17
9. Cross section of bottom condition for CFS test	18
10. Diagram of triaxial set-up	19
11. Types of failure	21
12. Comparison of deformation modes of W-K-U-3 and 4	23
13. Relationship of ϕ_ϵ and C_ϵ with strain	27
14. Stress-strain curves for unconfined tests	42
15. Stress-strain curves for unconfined tests	43
16. Stress-strain curves for unconfined tests	44
17. Stress-strain curves for unconfined tests	45
18. Stress-strain curves for unconfined tests	46
19. Stress-strain curves for unconfined tests	47
20. CFS curves for WF-CFS-2	59
21. CFS curves for WF-CFS-3	60
22. CFS curves for WF-CFS-4	61
23. CFS curves for WF-CFS-6	62
24. CFS curves for WF-CFS-7	63

Figure	Page
25. CFS curves for GF-CFS-1	64
26. CFS curves for GF-CFS-2	65
27. CFS curves for GF-CFS-3	66
28. CFS curves for GF-CFS-4	67
29. CFS curves for GF-CFS-5	68
30. Photographs of deformed specimens	74
31. Photographs of deformed specimens	75
32. Photographs of deformed specimens	76
33. Photographs of deformed specimens	77

LIST OF APPENDICES

Appendix		Page
A.	SAMPLE DATA SHEETS AND STRESS-STRAIN CURVES FOR UNCONFINED COMPRESSION TESTS	35
B.	SAMPLE DATA SHEETS AND CURVES FOR CFS TESTS .	48
C.	SAMPLE CALCULATIONS AND INTERPRETATION OF DATA	69
D.	PHOTOGRAPHS OF DEFORMED SPECIMENS	73

Notation

S	--	shear strength
σ	--	normal stress
σ_1	--	major principal stress
σ_3	--	minor principal stress
σ_{\max}	--	maximum compressive stress in unconfined compression test
τ	--	shear stress
C	--	cohesion
C_ϵ	--	cohesion, as determined from CFS test
ϕ	--	angle of internal friction
ϕ_ϵ	--	angle of internal friction, as determined from CFS test
ϵ	--	axial strain
ϵ_f	--	axial strain at failure
$\dot{\epsilon}$	--	strain rate
u	--	radial velocity
w	--	axial velocity
$\dot{\gamma}$	--	shear strain rate
Ψ	--	angle measured from a horizontal line through the center of a specimen
N	--	$\tan (45^\circ + \frac{\phi}{2})$
α	--	twice the angle between the principal directions of stress and strain
w	--	water content
L_0	--	length of sample at beginning of test
Δ_a	--	deviator stress, $(\sigma_1 - \sigma_3)$

I. INTRODUCTION

The shear strength of a soil as evaluated from a triaxial shear test is usually based on the Coulomb failure criterion. The strength is given by,

$$S = C + \sigma \tan \phi \quad (1)$$

in which S is the shear strength of the soil, C is a constant termed the cohesion, σ is the normal stress on the slip plane, and ϕ is a constant called the angle of internal friction.

In many cases, the failure surface is visible at the conclusion of a triaxial test. In other cases, examination of a failed sample shows no failure surface but only a general bulging of the specimen. In still other samples, a predominant failure plane is absent but many lesser slip lines are visible. The effect of the type of failure on the shear strength and on the friction and cohesion of a soil is not fully understood.

Haythornthwaite (1959, 1963) applied the plasticity theory to calculate the velocity field in a triaxial sample and showed that the solution is not unique. He states that a stress-strain relation in addition to the failure criterion would be required to establish uniqueness.

The purpose of this study is to evaluate the deformation conditions that accompany failure and their effect on the failure criterion.

II. THEORETICAL CONSIDERATIONS

2.1 Failure surface

The relationship given by the Coulomb equation (1) produces a straight line when shear stress is plotted against normal stress. Stresses at failure can be represented on the same plot by a circle with the center at $(\tau = 0, \sigma = \frac{\sigma_1 + \sigma_3}{2})$ and a diameter of $(\sigma_1 - \sigma_3)$, where σ_1 and σ_3 are the major and minor principal stresses respectively (see Fig. 1).

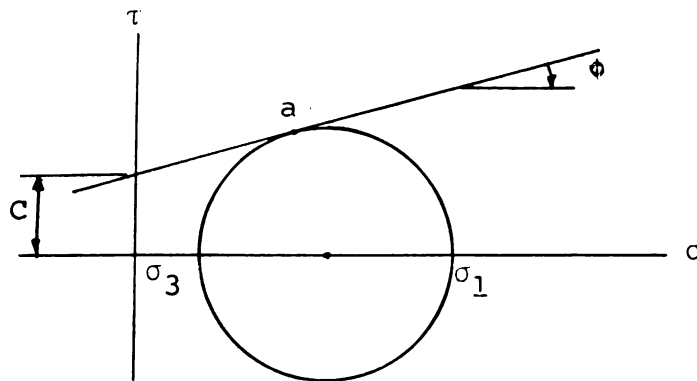


Fig. 1. Mohr circle.

The straight line defined by equation (1) is known as the failure envelope and the circle is known as the Mohr circle. Failure is represented by the point of tangency, a , between the circle and the failure envelope.

In a conventional triaxial test, the friction of the end plates does not permit the soil in contact with the

plates to expand in a radial direction. Rowe (1964) pointed out that this produces dead zones at the ends of the sample as shown in Fig. 2. This restricts lateral strain to the middle portion of the specimen and causes failure to occur within narrow zones. This often results in the formation of a single slip surface.

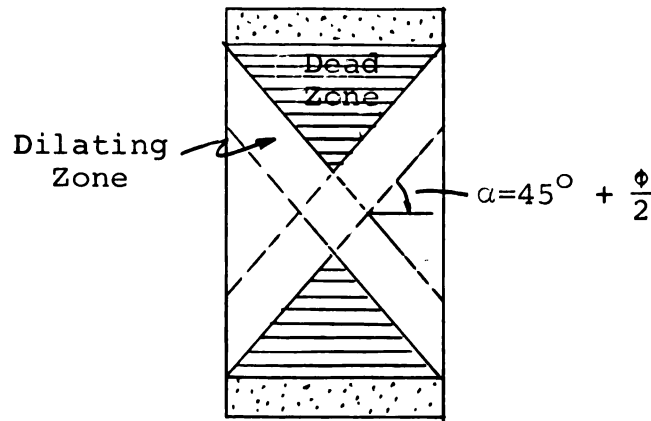


Fig. 2. Formation of dead zones.

Rowe (1964) notes that the use of frictionless end plates would eliminate the dead zones and thus tend to prevent the formation of a predominant failure surface. He explains that without the dead zones, uniform lateral strain results and there is no longer a tendency for one zone to fail before another. He predicts that this causes the sample to reach larger strains before failure and that the failure occurs in the form of multiple failure surfaces.

2.2 Plasticity solutions for axial symmetry

Haythornthwaite (1959) used the theory of plasticity to calculate the velocity fields during a triaxial test.

In his solution, the soil is assumed to be an isotropic, ideally plastic material. Due to the assumption of isotropy, the principal direction of strain coincides with the principal direction of stress. Thus the shear strain rate in the r-Z plane, $\dot{\gamma}_{rZ}$, must be zero. This can be written as,

$$\dot{\gamma}_{rZ} = \frac{\partial u}{\partial Z} + \frac{\partial w}{\partial r} = 0, \quad (2)$$

where u and w are the radial and axial velocities respectively. The other strain rate components are,

$$\dot{\epsilon}_r = \frac{\partial u}{\partial r}; \quad \dot{\epsilon}_\theta = \frac{u}{r}; \quad \dot{\epsilon}_Z = \frac{\partial w}{\partial Z} \quad (3)$$

According to the plastic potential theory, the strain rate components must satisfy the relationship,

$$\dot{\epsilon}_r + \dot{\epsilon}_\theta + \dot{\epsilon}_Z \tan^2 (45^\circ + \frac{\phi}{2}) = 0 \quad (4)$$

Substituting (3) into (4),

$$\frac{\partial u}{\partial r} + \frac{u}{r} + \frac{\partial w}{\partial Z} \tan^2 (45^\circ + \frac{\phi}{2}) = 0 \quad (5)$$

Equations (2) and (5) are the governing differential equations.

These equations are first solved using the boundary conditions shown in Fig. 3. The rigid zones shown at both ends are the result of the end restraint. Continuity of velocity is assumed across OB so that $u = w = 0$ on OB except at 0. Using these boundary conditions, the solution of the differential equation is,

$$\left. \begin{aligned} u &= \frac{2}{\pi} \sqrt{N^2 - \tan^2 \Psi} \\ w &= \frac{2}{\pi} \tan^{-1} \sqrt{N^2 \cot^2 \Psi - 1} \end{aligned} \right\} \quad (6)$$

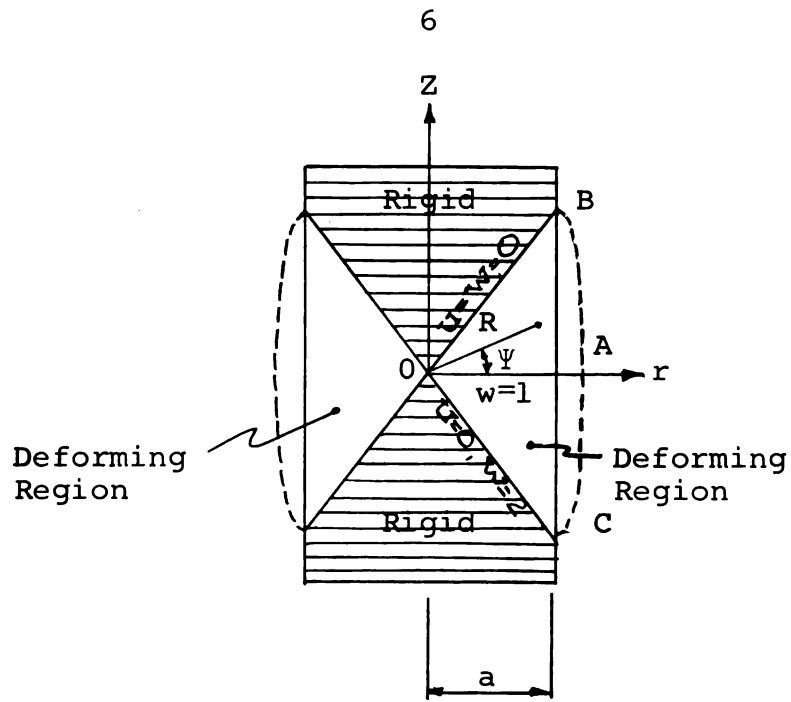


Fig. 3. Sketch of deforming region for Eq. (6).

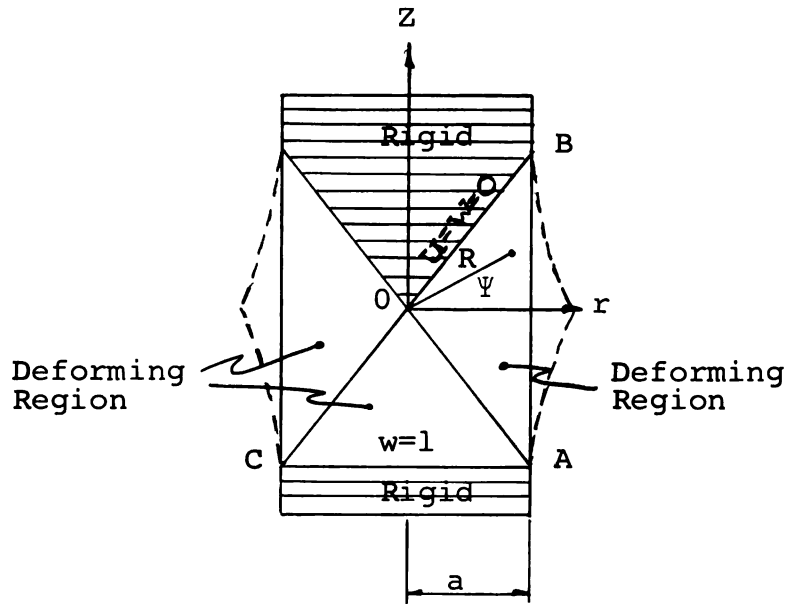


Fig. 4. Sketch of deforming region for Eq. (8).

where $N = \tan (45^\circ + \frac{\phi}{2})$.

The nature of the deformation defined by (6) is shown by the dotted lines in Fig. 3.

In order to show that the deformation defined by equations (6) is not the only possible mode of deformation for the axially symmetric case, Haythornthwaite solves equations (2) and (5) using the boundary conditions shown in Fig. 4. In region OAC, the field used is

$$\left. \begin{aligned} u &= \frac{r}{2a} \tan (45^\circ + \frac{\phi}{2}) \\ w &= -\frac{z}{2a} \tan (45^\circ + \frac{\phi}{2}) \end{aligned} \right\} \quad (7)$$

Equations (7) satisfy (2) and (5) and also the boundary condition $w = 1$ on AC. The solution for region AOB, using the boundary conditions of Fig. 4 is,

$$\left. \begin{aligned} u &= \frac{R [N^2 \cos \Psi \tan^{-1} \sqrt{N^2 \cot^2 \Psi - 1} - \sin \Psi \sqrt{N^2 - \tan^2 \Psi}]}{2\pi a N} \\ w &= \frac{R [\cos \Psi \sqrt{N^2 - \tan^2 \Psi} - \sin \Psi \tan^{-1} \sqrt{N^2 \cot^2 \Psi - 1}]}{\pi a N} \end{aligned} \right\} \quad (8)$$

The deformation described by equations (8) is shown by the dotted line in Fig. 4. In equations (6) and (8) Ψ varies from 0° to $(45^\circ + \frac{\phi}{2})$.

2.3 Solution for axial symmetry by kinematics

Saint-Venant's Principle states that the principal direction of strain coincides with the principal direction of stress. By an analysis of the kinematics along the slip

planes, de Jong (1958) proves that this is true at failure only for a material with $\phi = 0$. For a material with $\phi > 0$, the angle between the principal directions of stress and strain may be anywhere between zero and ϕ . Haythornthwaite (1963) proves the same thing using a different approach.

Haythornthwaite (1963) presents another solution for axial symmetry in which he assumes an angle of $\alpha/2$ between the principal directions of stress and strain. From the geometry of the Mohr circle for strain, the following relationship holds;

$$\tan \alpha = \frac{\dot{\gamma}_{rZ}}{\dot{\epsilon}_r - \dot{\epsilon}_Z} \quad (9)$$

With the definitions

$$\dot{\epsilon}_r = \frac{\partial u}{\partial r} ; \dot{\epsilon}_\theta = \frac{u}{r} ; \dot{\epsilon}_Z = \frac{\partial w}{\partial Z} \quad (3)$$

and $\dot{\gamma}_{rZ} = \frac{\partial u}{\partial Z} + \frac{\partial w}{\partial r}$ (10)

(9) becomes

$$\tan \alpha \frac{\partial u}{\partial r} - \frac{\partial u}{\partial Z} - \frac{\partial w}{\partial r} - \tan \alpha \frac{\partial w}{\partial Z} = 0 \quad (11)$$

The zero dilation equation is

$$\frac{\partial u}{\partial r} + \frac{u}{r} + \frac{\partial w}{\partial Z} = 0 \quad (12)$$

Equations (11) and (12) are the governing differential equations. It can be noted here that if the principal directions of stress and strain coincide ($\alpha = 0$) as is assumed in the plasticity solution of Sec. 2.2, equation (11) degenerates to equation (2) which is one of the governing differential equations in the plasticity solution. Equations (11) and (12) are solved using the boundary conditions shown in Fig. 5.

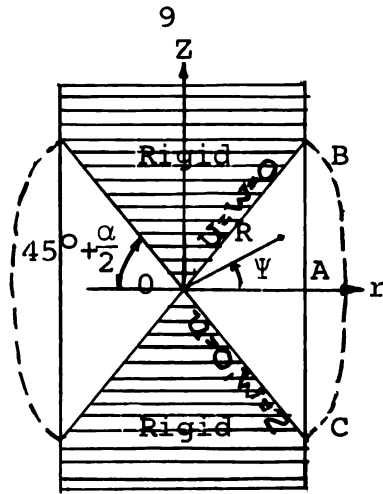


Fig. 5. Sketch of deforming region for Eq. (13).

The solution of (11) and (12) is

$$\left. \begin{aligned}
 u &= \frac{\cos^2 \alpha \sqrt{\frac{N - \tan \Psi}{N + \tan \Psi}}}{\frac{\pi}{2} + \alpha + \frac{1}{2} \sin 2 \alpha} \\
 w &= \frac{\frac{\pi}{2} - \sin^{-1} (\tan \Psi \cos \alpha - \sin \alpha) + \frac{1}{2} \sin 2 \alpha \sqrt{\frac{N - \tan \Psi}{N + \tan \Psi}}}{\frac{\pi}{2} + \alpha + \frac{1}{2} \sin 2 \alpha}
 \end{aligned} \right\} (13)$$

$$\text{where } N = \tan \left(45^\circ + \frac{\phi}{2} \right)$$

and Ψ varies from 0° to $(45^\circ + \frac{\phi}{2})$. The deformation pattern described by (13) is shown by the dotted lines in Fig. 5.

III. EXPERIMENTAL PROGRAM

The experimental program is designed to observe the deformation characteristics of specimens at failure and their effect on the shear strength parameters. The variables studied are the strain rate and the end restraint.

3.1 Soils used

There are three different clays used in the testing program. The first is a glacial lake clay taken from a site near Sault Ste. Marie, Michigan, at a depth of approximately 5 feet below the ground surface. This is referred to as Sault clay. The Sault clay contains about 50 percent illite, 25 percent vermiculite, and 15 percent chlorite. The remaining 10 percent is a combination of montmorillonite, quartz, feldspar, and kaolinite according to X-ray diffraction tests (Dillon, 1963). The other two soils used are commercial grundite and kaolinite. The index properties of the soils used are given in Table 1.

Table 1. Index properties.

Type Soil	Plastic Limit	Liquid Limit	Plasticity Index	Clay Fraction
Sault	23.6%	60.5%	36.9%	0.60
Grundite	25.0%	78.0%	53.0%	0.65
Kaolinite	28.0%	50.0%	22.0%	

3.2 Preparation of samples

The Sault clay and grundite samples are compacted and trimmed as described by Holliday (1963). Due to the difficulty in trimming, the kaolinite samples are prepared differently. The dry clay is mixed with enough distilled water to make a water content of approximately 25 percent. After the clay and water are thoroughly mixed, the mixture is compacted in the Harvard Compaction mold in 5 layers. Each layer is tamped 25 times evenly over the surface. The force delivered by the tamper is 50 pounds over a circular area of .15 square inch.

Specimens that are referred to as "compacted" are those prepared in one of the two ways mentioned above. The term "remolded" as used in this report means that the sample is remolded by hand immediately prior to trimming.

3.3 Unconfined compression tests

Haythornthwaite (1963) pointed out that while the final deformation pattern of a triaxial sample is well known, it is not clear exactly how the deformation proceeds during the test. In order to study the deformation patterns of clay samples, photographs are taken at various strains throughout a series of tests. The photographs are taken by a camera that is mounted on a frame in front of the triaxial cell. Initial plans were to take photographs during triaxial tests. However, this proved unsuccessful due to the fact that the lucite of the triaxial cell and

the water within the cell prevented accurate focusing. It was then decided to remove the lucite cell and run unconfined compression tests.

In the first unconfined compression tests (W - C - CU - 2 and W - C - CU - 3), the sample was first consolidated under a hydrostatic pressure of 2.00 kilograms per square centimeter. The pressure was then relieved, the water drained out, and the lucite cell removed. The photographs showed that most of the deformation took place at the bottom of the sample. Upon checking the final water content, it was determined that the water content was higher at the bottom of the sample. Table 2 shows the moisture content variation within the sample.

Table 2. Final water content variation for consolidated samples.

Test Designation	Initial Water Content-%	Final Water Content - %		
		Top	Middle	Bottom
W-C-CU-2	40.8	30.1	31.8	32.8
W-C-CU-3	41.9	28.8	30.7	32.6

The higher water content at the bottom is probably due to the absorption of water from the porous stone as the specimen tends to swell upon release of pressure. It seems reasonable, therefore, that the large deformation at the bottom is the result of non-homogeneity rather than a failure characteristic. On the basis of this, it was determined to run tests on samples immediately after trimming without consolidation.

"Frictionless" end plates are used in order to determine their effect on the mode of failure and on the shear strength. The end plates are made of lucite and are approximately 2 inches in diameter. The bottom end plate is cut out at the bottom so that it fits over the pedestal of the triaxial cell. Two small holes that line up with the holes in the pedestal are drilled through the bottom end plate. The frictionless condition is obtained by sprinkling graphite on to the lucite end plates and then placing a thin rubber membrane over it. The top and bottom of the sample are then in contact with a rubber membrane which is free to expand in the radial direction due to the graphite. This is illustrated in Fig. 6.

Unconfined compression tests are run on both kaolinite and Sault clay. Most of the tests are run at a constant strain rate with several different strain rates being used. In order to obtain an extremely fast strain rate, an instantaneous load is applied in two of the tests (W-S-U-10 and W-S-U-11). This is done by placing an 8 kilogram weight on to a loading yoke as shown in Fig. 7. Photographs are taken in selected tests. A summary of the test program on the kaolinite is given in Table 3 and on the Sault clay in Table 4.

Stress-strain curves are obtained in each test. The maximum compressive stress (σ_{\max}) and the strain at which the maximum compressive stress occurs (ϵ_f) are determined. The deformation patterns are studied by overlaying the

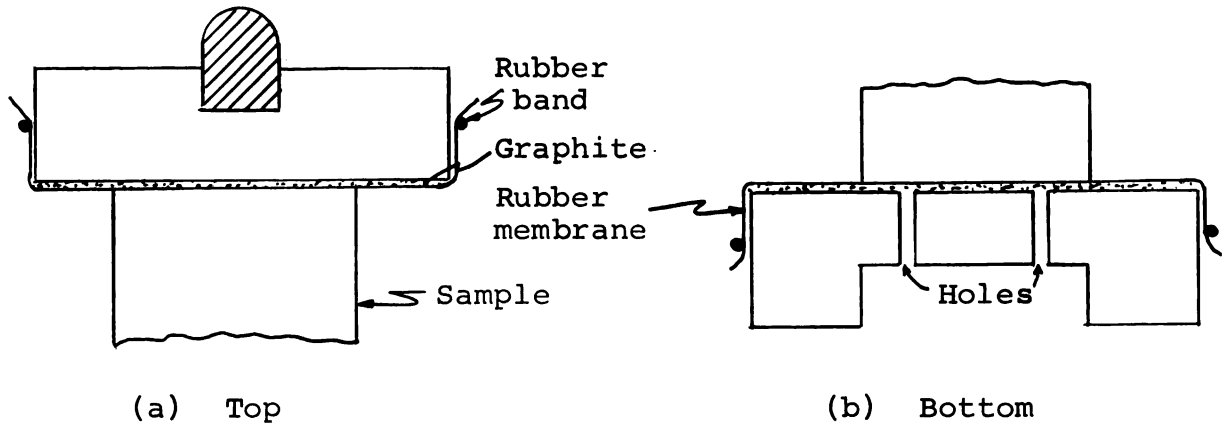


Fig. 6. Cross section of frictionless end plates.

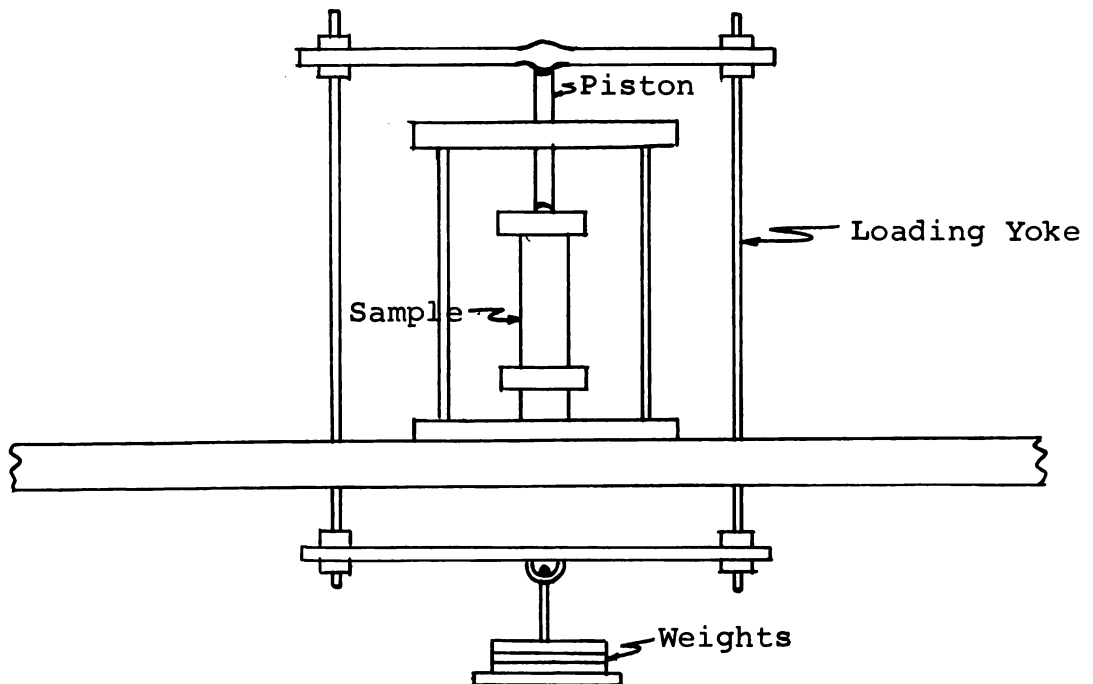


Fig. 7. Set-up for instantaneous load application.

photographs taken at different strains. The type of failure is noted in each test.

Table 3. Summary of testing program on kaolinite.

Test Designation	Water Content W - %	Strain Rate $\dot{\epsilon}$ - %/Hr.	Type of End Plate	Length L_0 - in.
W-K-U-1*	24.8	360	Conventional	2.8
W-K-U-2*	25.3	360	Conventional	2.8
W-K-U-3*	26.1	360	Conventional	2.8
W-K-U-4*	23.8	0.23	Conventional	2.8
W-K-U-5*	25.9	360	Frictionless	2.8
W-K-U-6*	26.2	360	Frictionless	2.8
W-K-U-7*	25.9	360	Conventional	2.8
W-K-U-8*	25.2	0.40	Frictionless	2.8
W-K-U-9	26.1	700	Frictionless	1.4
W-K-U-10	26.1	700	Frictionless	1.4
W-K-U-11	26.1	360	Frictionless	2.8

*Photographs taken.

3.4 CFS tests

The CFS tests follow the same technique as that described by Schmertmann and Osterberg (1960). It is a triaxial test in which the cohesion (C_ϵ) and angle of friction (ϕ_ϵ) are determined at various strains throughout the loading process. The procedures used are described below.

After the sample is trimmed and cut to a length of 2.8 inches, three wool yarns are placed lengthwise through the sample using a needle. This is essential to quick response to pore pressure changes and to rapid consolidation.

Table 4. Summary of unconfined testing program on Sault clay.

Test Designation	Preparation	Water Content w - %	Strain Rate $\dot{\epsilon}$ - %/Hr.	Type of End Plate	Length L_0 - in.
W-S-U-1*	Remolded	40.8	400	Frictionless	2.8
W-S-U-2*	Remolded	40.0	400	Frictionless	2.8
W-S-U-3	Compacted	39.5	400	Conventional	2.8
W-S-U-4	Remolded	37.7	400	Conventional	2.8
W-S-U-5	Remolded	36.4	400	Frictionless	2.8
W-S-U-6	Remolded	39.0	400	Frictionless	2.8
W-S-U-7	Remolded	39.0	400	Frictionless	2.8
W-S-U-8	Remolded	39.0	400	Frictionless	2.8
W-S-U-9	Remolded	39.0	400	Frictionless	2.8
W-S-U-10	Remolded	39.0	40,000	Frictionless	2.8
W-S-U-11	Remolded	39.0	40,000	Frictionless	2.8
W-C-CU-2*	Consolidated	(See Table 2)	4.7	Conventional	2.64
W-C-CU-3*	Consolidated	(See Table 2)	300	Conventional	2.64

*Photographs taken.

With the frictionless bottom end plate, it is necessary to connect the yarns with the holes in the end plate to ensure proper drainage. This is done by placing the ends of two of the yarns so as to line up with one of the holes in the end plate and the third yarn to line up with the other hole. This is shown in Fig. 8.

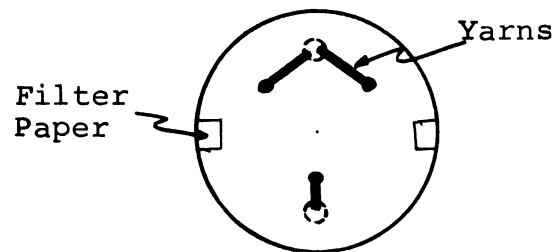


Fig. 8. Sketch of bottom of triaxial sample.

A 1/4 inch wide piece of filter paper is placed on each side of the sample to further speed up consolidation. The sample is then weighed and placed between the end plates. It is covered with two rubber membranes, each of which is secured at each end by at least two rubber bands. The sample is then placed in the triaxial cell by fitting the bottom end plate over the pedestal. A third membrane, which had been secured to the bottom of the pedestal by rubber bands, is then stretched over the bottom end plate and rubber bands are stretched over the outside of this membrane. This bottom condition is shown in Fig. 9.

All samples are consolidated under a pressure of 2 kilograms per square centimeter for 24 hours. A back pressure of 2 kilograms per square centimeter is then applied for 24 hours. A pore pressure change of 0.5

kilograms per square centimeter is applied periodically in order to obtain the two stress-strain curves of the CFS test. Thus, the effective major principal stress ($\bar{\sigma}_1$) alternates between 2.0 and 1.5 kilograms per square centimeter. For a detailed description of the procedure, see Holliday (1963). A diagram of the triaxial set up is given in Fig.10.

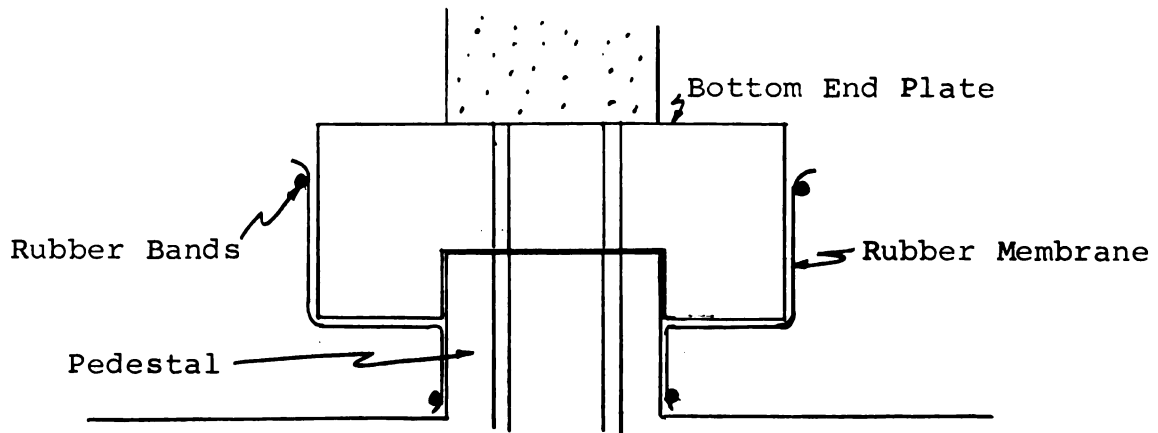


Fig. 9. Cross section of bottom condition for CFS test.

CFS tests are run on both grundite and Sault clay compacted samples. Frictionless end plates are used in all CFS tests in this study. Due to the uniform deformation caused by the smooth ends, each CFS test is carried out to a strain of at least 40 percent. This allows ϕ_ϵ and C_ϵ to be calculated at large strains. The pore pressure is continually adjusted to balance the deviator stress, with one exception. In the slower strain rate tests, it is necessary for the test to run overnight. In this case, valve C (Fig. 10) is closed at night and reopened in the morning. It should be noted that the pore pressure usually varies only slightly overnight and is easily readjusted in the morning.

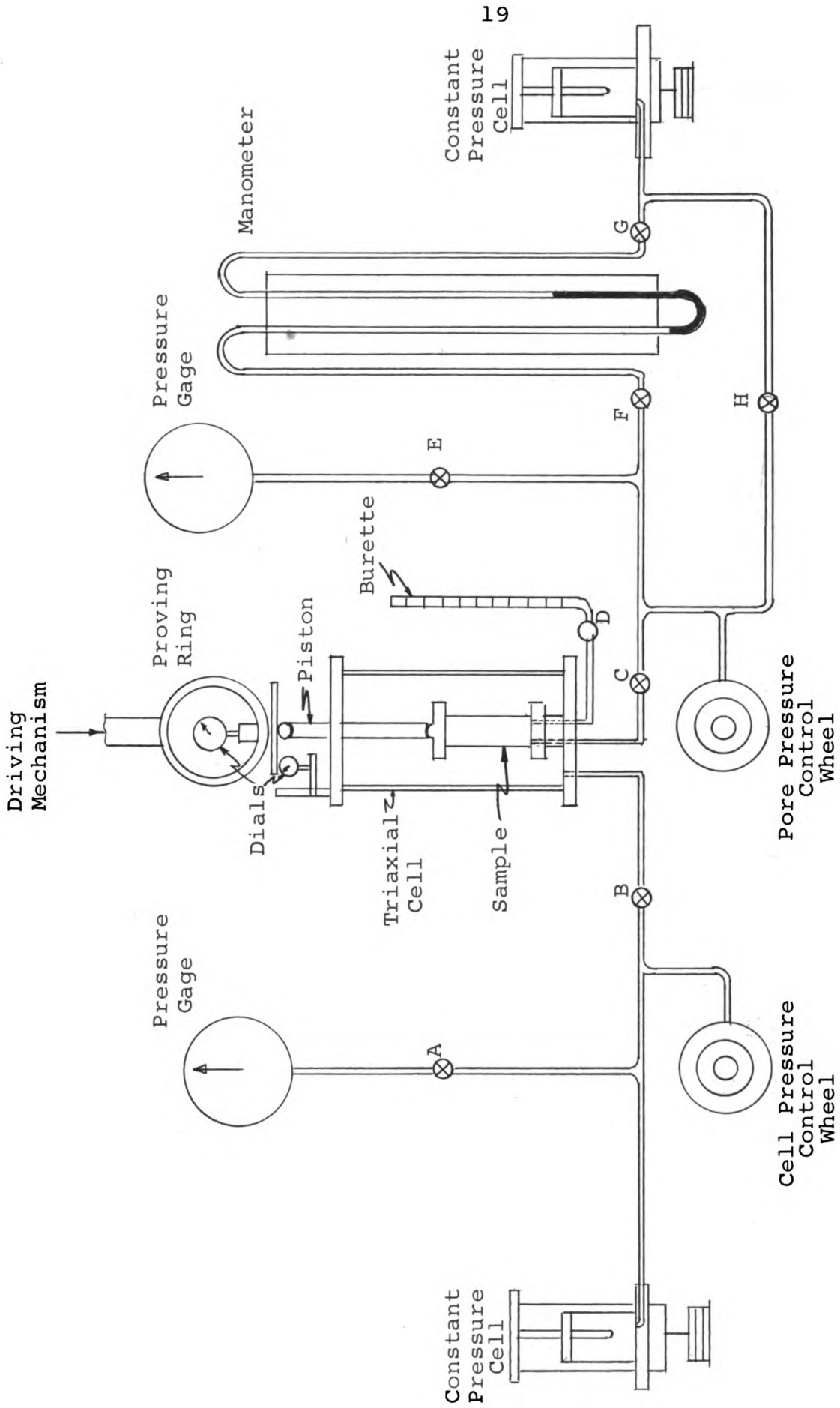


Fig. 10. Diagram of triaxial set up.

Using the two stress-strain curves from each test, ϕ_ϵ and C_ϵ are calculated at several strains according to the method shown in Appendix B. ϕ_ϵ and C_ϵ are plotted against strain to determine their relationship and the type of failure is noted in each test. Table 5 gives a summary of the CFS tests.

Table 5. Summary of CFS tests.

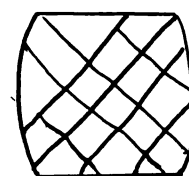
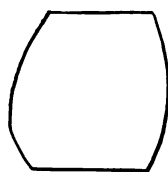
Test Designation	Clay	Avg. Strain Rate $\dot{\epsilon}$ - %/Hr.	Initial Water Content w_i - %
WF-CFS-2	Sault	1.25	42.3
WF-CFS-3	Sault	1.28	40.8
WF-CFS-4	Sault	1.25	42.0
WF-CFS-6	Sault	6.12	42.0
WF-CFS-7	Sault	5.93	40.2
GF-CFS-1	Grundite	1.24	40.9
GF-CFS-2	Grundite	1.24	40.8
GF-CFS-3	Grundite	7.06	40.9
GF-CFS-4	Grundite	4.94	40.8
GF-CFS-5	Grundite	1.26	41.4

IV. PRESENTATION AND DISCUSSION OF RESULTS

The results of the unconfined compression tests on kaolinite and Sault clay are tabulated in Tables 6 and 7 respectively. Similarly, Tables 8 and 9 summarize the CFS test results.

4.1 Failure types

The types of failure encountered in this study can be classified into three main groups. The three types, failure plane, bulging, and multiple slip lines are sketched in Fig. 11.



(a) Failure plane

(b) Bulging

(c) Multiple slip lines

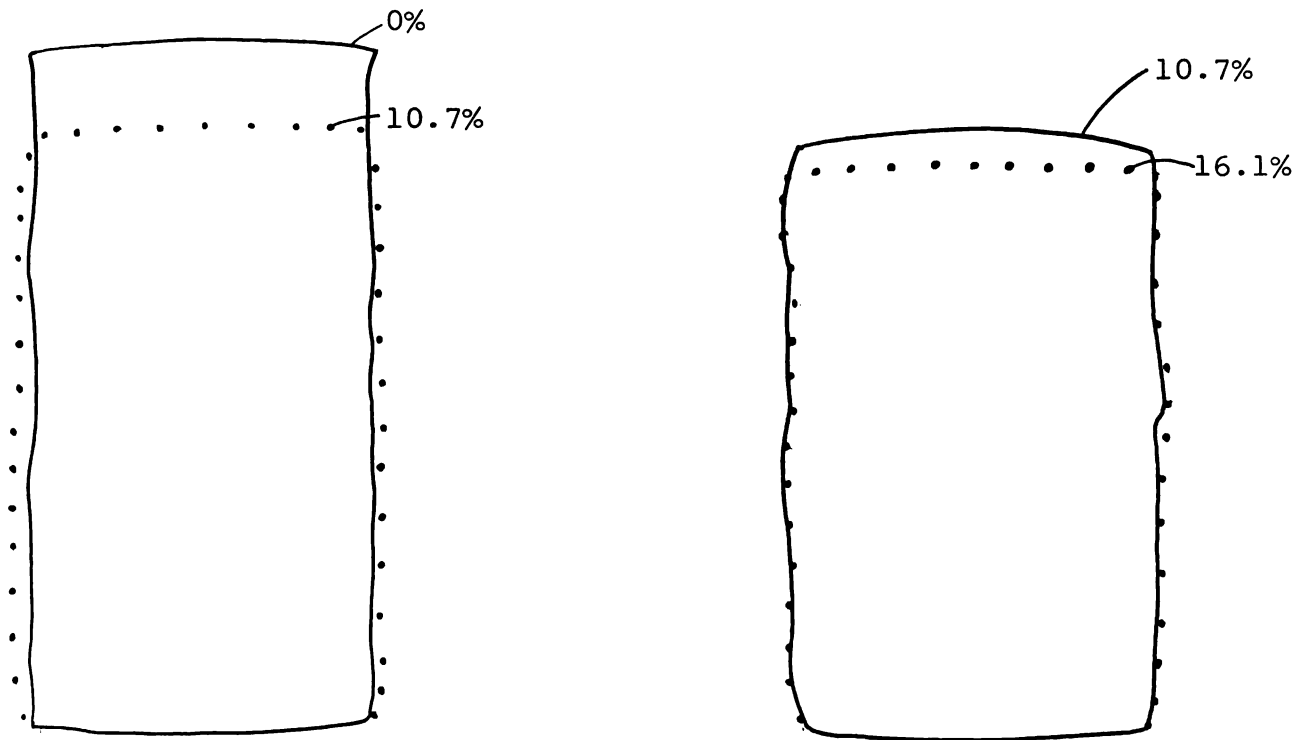
Fig. 11. Types of failure.

In cases where either a failure plane or slip lines appear, they become visible shortly after the maximum stress is reached. For kaolinite, the maximum stress usually occurs at about 15% strain. In all of the kaolinite tests on standard length (2.8 inches) samples, the photographs show bulging until shortly after this peak stress is reached. A single failure plane then develops and further

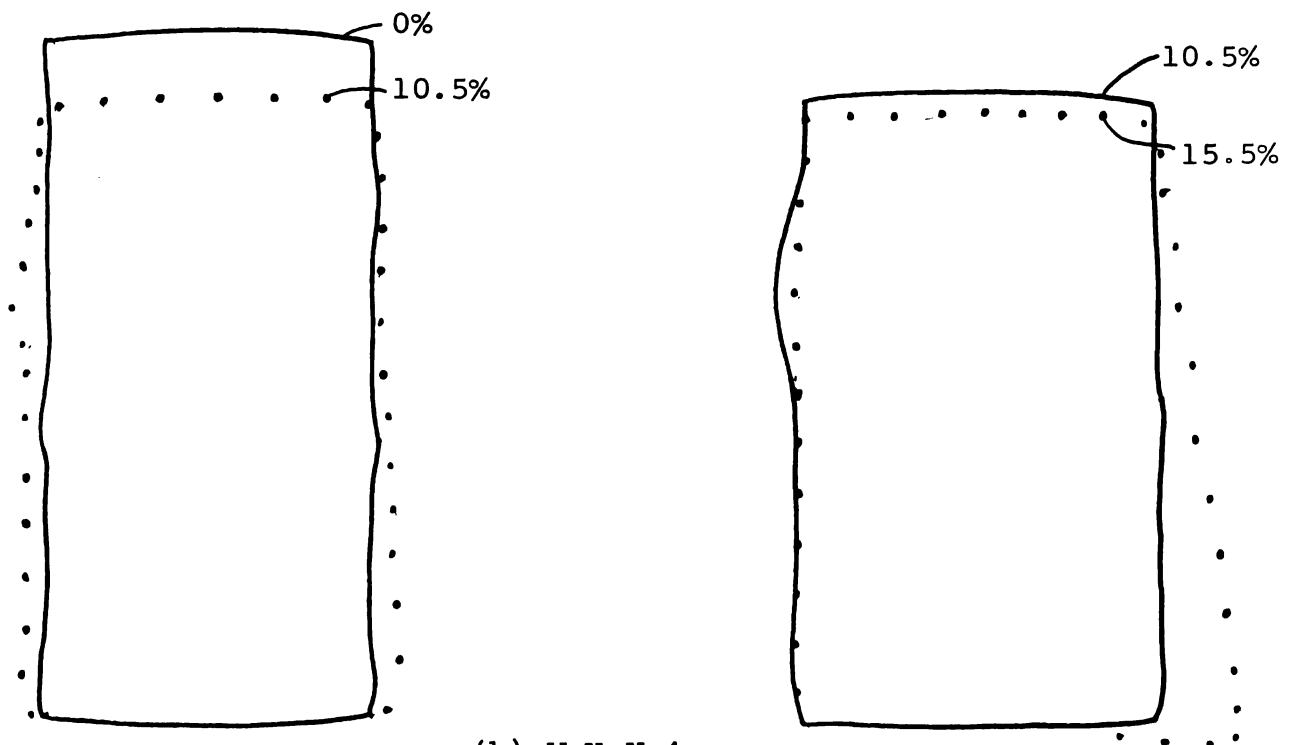
motion is limited to rigid body movement along the failure surface. This is particularly apparent upon comparing the photographs of W-K-U-3 and W-K-U-4 (see Fig. 12). The photographs at early strains show the same general bulging in each test. Later photographs in W-K-U-4 show large rigid body movement of the right side downward with respect to the left side. This is readily visible since the movement took place perpendicular to the direction of the photographs. In W-K-U-3, photographs at later strains show no change; although, it is obvious that a large amount of sliding took place parallel to the direction of the photographs. This shows that all of the movement is along the failure plane, probably because there is a reduction in area along that section as soon as the failure plane develops.

By using shorter specimens (1.4 inches) in tests W-K-U-10 and W-K-U-11, formation of a single failure plane is prevented. Thus, there is no area reduction and failure in the form of multiple slip lines occurs at a larger strain (25% \pm).

Since a single failure plane develops at such low strains in the 2.8 inch kaolinite specimens, the type of end plate does not affect the type of failure. In the case of the unconfined compression tests on the Sault clay, however, a failure plane does not develop at low strains and, therefore, the type of end restraint has a marked effect on the failure type. For example, in most of the tests (W-S-U-3 and 4, W-C-CU-3) with the conventional



(a) W-K-U-3



(b) W-K-U-4

Fig. 12. Comparison of deformation modes of W-K-U-3 and 4 (taken from photographs).

end plates, gross distortion was noted in the form of bulging near the center of the sample. Either a peak stress is reached at a strain of about 25% or the stress-strain curve is still rising at the conclusion of the test (see Table 7). Frictionless ends, however, allow large strains without too much bulging of the specimen and multiple slip lines form at strains of 35% \pm in most tests. This result, coupled with the results of the kaolinite tests on short specimens, indicates that if area reduction due to sliding along a single failure plane or bulging at the center can be prevented by the use of shorter specimens and frictionless end plates, failure occurs at greater strains in the form of multiple slip lines.

The strain at which slip lines develop was found to be sensitive to strain rate. Slip planes form at greater strains as the strain rate increases. This is particularly apparent from the results of the unconfined compression tests on the Sault clay. This trend is not as clear in the tests on kaolinite.

The results of the CFS tests with frictionless end plates show two trends relating to conditions affecting the type of failure. First, single failure planes appear only in those tests in which the top end plate tilted. This is believed to be due to the fact that the tilted end plates produce non uniform stress distribution thus causing failure along the failure surface. Hence, this is not considered to be representative of the soil behavior. Multiple slip

lines occur in each test on the Sault clay (even though the top end plate tilted in WF-CFS-2). Most of the failures on the grundite involve tilting of the top end plate and are combinations of A and C types. This indicates that had tilting not occurred, multiple slip lines might have developed at larger strains.

While the photographs help to gain insight into the deformation conditions that accompany failure, it is difficult to measure the exact magnitude of the bulging from the photographs since the bulging takes place only at small strains in most tests. Therefore, it is difficult to confirm or reject any of the solutions given in Chapter II. In cases where the bulging continues to large strains, the change in stress distribution due to the bulge would make the solutions of questionable value. It can be noted, however, that bulging occurs throughout the entire length of the sample and is not confined to the zones predicted by Haythornthwaite's solutions (in the rough end tests).

4.2 Effect on strength

The strength depends on the strain rate and the type of end restraint. The strain rate effect is particularly apparent in the CFS tests and unconfined compression tests W-C-CU-2 and W-C-CU-3. Comparison of these tests, in which other variables are held constant, clearly shows that the strength increases as the strain rate increases. Further examination of the CFS test results shows that as the strain rate increases, the cohesion (C_c) increases while

the angle of friction (ϕ_c) decreases. More tests at different strain rates would be necessary to determine the relationship between the shear strength parameters and strain rate.

The strength is greater in the tests in which frictionless end plates are used. This is best exemplified by comparing tests W-S-U-1 and 2 with W-S-U-3 and 4. The former pair of tests with frictionless end plates, shows greater strength even though the tests are similar in all other respects. Comparison of the CFS test results with those obtained by A. K. Loh at Michigan State University using conventional end plates show the same trend. This is believed to be due to the fact that the frictionless ends produce a more uniform stress distribution and deformation mode, thus preventing a premature failure caused by stress concentrations in certain portions of the specimen.

Since the frictionless end plates produce fairly uniform deformation even at large strains, it is possible to measure the shear strength parameters to a strain of 40%. These relationships are shown in Fig. 13 (for results of specific tests, see Appendix B). The angle of friction increases with strain as shown in Fig. 13(a). Most of the friction is developed before the strain reaches 10 percent but in most cases it continues to rise at larger strains. The cohesion reaches a peak between 5 and 13 percent strain and then decreases to a constant value at large strains. The strain at which the peak cohesion

Table 6. Results of unconfined compression tests on kaolinite.

Test Designation	Water Content w - %	Strain Rate $\dot{\epsilon}$ - %/Hr.	Type of End Plate	Length L_0 - in.	Peak Stress σ_{max} - Kg/Cm ²	Strain at Peak Stress ϵ_f - %	Type of Failure*
W-K-U-1	24.8	360	Conventional	2.8	5.05	13.5	A
W-K-U-2	25.3	360	Conventional	2.8	4.00	20	B & C
W-K-U-3	26.1	360	Conventional	2.8	3.60	15	A
W-K-U-4	23.8	0.23	Conventional	2.8	4.00	10.5	A
W-K-U-5	25.9	360	Frictionless	2.8	6.40	9	A
W-K-U-6	26.2	360	Frictionless	2.8	3.90	21.5	A
W-K-U-7	25.9	360	Conventional	2.8	3.30	16.5	A
W-K-U-8	25.2	0.40	Frictionless	2.8	1.50	11.5	A
W-K-U-9	26.1	700	Frictionless	1.4	3.25	25	C
W-K-U-10	26.1	700	Frictionless	1.4	4.00	21.5	C
W-K-U-11	26.1	360	Frictionless	2.8	3.85	18	A

*Types of Failure:

A -- Single Failure Plane

B -- Bulging

C -- Multiple Slip Lines

Table 7. Results of unconfined compression tests on Sault clay.

Test Designation	Water Content w - %	Strain Rate $\dot{\epsilon}$ -%/Hr.	Type of End Plate	Preparation	Length L_0 - in	Peak Stress σ_{max} - Kg/Cm ²	Peak Stress ϵ_f - %	Type of Failure*
W-S-U-1	40.8	400	Frictionless	Remolded	2.8	0.375	35	C
W-S-U-2	40.0	400	Frictionless	Remolded	2.8	0.355	36	C
W-S-U-3	39.5	400	Conventional	Compacted	2.8	0.240	30	B & C
W-S-U-4	37.7	400	Conventional	Remolded	2.8	0.250	23	A
W-S-U-5	36.4	400	Frictionless	Remolded	2.8	0.285	35	C
W-S-U-6	39	400	Frictionless	Remolded	2.8	0.210**	32**	--
W-S-U-7	39	400	Frictionless	Remolded	2.8	0.310**	37**	C
W-S-U-8	39	400	Frictionless	Remolded	2.8	0.370**	40**	C
W-S-U-9	39	400	Frictionless	Remolded	2.8	0.400**	40**	C
W-S-U-10	39	40,000	Frictionless	Remolded	2.8	***	50	B & C
W-S-U-11	39	40,000	Frictionless	Remolded	2.8	***	50	C
W-C-CU-2	(See Table 2)	4.7	Conventional	Consolidated	2.64	1.10	9	A & B
W-C-CU-3	(See Table 2)	300	Conventional	Consolidated	2.64	1.75**	18**	B

*Types of Failure: A - Single Failure Plane
 B - Bulging
 C - Multiple Slip Lines

**Peak not reached -- values given are "end of test" values.

***Instantaneous 8 K_G load applied.

Table 8. Summary of CFS results.

Test Designation	Type of Clay	Avg. Strain Rate $\dot{\epsilon}$ -%/Hr.	Initial Water Content w_i - %	Final Water Content w_f - %	Max. Deviator Stress $(\sigma_1 - \sigma_3)$ - Kg/Cm ²	Strain at Failure ϵ_f - %	Type of Failure*
WF-CFS-2	Sault	1.25	42.3	32.0	1.36	12.5	C**
WF-CFS-3	Sault	1.28	40.8	32.2	1.38	13	C
WF-CFS-4	Sault	1.25	42.0	32.1	1.34	13	C
WF-CFS-6	Sault	6.12	42.0	32.2	1.405	13	C
WF-CFS-7	Sault	5.93	40.2	32.9	1.44	11.5	C
GF-CFS-1	Grundite	1.24	40.9	32.3	1.26	9	A & C**
GF-CFS-2	Grundite	1.24	40.8	32.5	1.295	11	A & C
GF-CFS-3	Grundite	7.06	40.9	32.6	1.455	10	A**
GF-CFS-4	Grundite	4.94	40.8	32.9	1.45	9	B & C
GF-CFS-5	Grundite	1.26	41.4	32.7	1.29	6.5	A & C**

*Types of Failure:

A - Single Failure Plane

B - Bulging

C - Multiple Slip Lines

**Top End Plate Tilted.

Table 9. Summary of CFS results on ϕ_{ϵ} and C_{ϵ} .

Test Designation	Avg. Strain Rate ϵ -%/Hr.	ϕ_{ϵ} at		ϕ_{ϵ} at 40% Strain	$\frac{\phi_{40}}{\phi_{10}}$	Max ϕ_{ϵ} -Deg.	Max C_{ϵ} -Kg/Cm ²	Strain at C_{ϵ} max.
		ϕ_{10} -Degrees	ϕ_{40} -Degrees					
WF-CFS-2	1.25	13	18.4	18.4	1.415	18.4	.47	6
WF-CFS-3	1.28	11.7	14.0	14.0	1.197	14.0	.485	5
WF-CFS-4	1.25	8.82	10.2	10.2	1.156	12.4	.475	7
WF-CFS-6	6.12	6.6	8.14	8.14	1.232	8.68	.58	12.5
WF-CFS-7	5.93	6.45	7.76	7.76	1.202	8.57	.58	10
GF-CFS-1	1.24	6.10	6.6	6.6	1.082	6.96	.495	8.5
GF-CFS-2	1.24	3.73	5.95	5.95	1.595	5.95	.565	8.5
GF-CFS-3	7.06	1.90	1.77	1.77	.932	2.33	.685	10
GF-CFS-4	4.94	2.95	1.95	1.95	.662	3.08	.66	10
GF-CFS-5	1.26	6.16	4.78	4.78	.775	7.54	.532	5

V. CONCLUSIONS

The following conclusions may be drawn from the test results.

- a. After a single failure plane develops, further deformation is limited to rigid body sliding along the failure surface since that section experiences an area reduction.
- b. If gross distortion of the specimen can be prevented by using frictionless end plates and shorter samples, failure occurs at a greater strain in the form of multiple slip lines.
- c. The strain at which slip lines appear increases as the strain rate increases.
- d. The strength increases with strain rate.
- e. The unconfined compressive strength, cohesion and friction are all higher when frictionless end plates are used.
- f. The strain at which the peak cohesion occurs increases as the strain rate increases.

On the basis of this study, it is suggested that further investigations be carried out on these subjects.

- a. The use of frictionless end plates and shorter samples should be investigated further to determine their general usefulness.

- b. Tests should be run at different strain rates so that the relationship between the appearance of slip lines and strain rate can be established.
- c. Tests similar to those used in this study should be conducted on other soils to determine the general application of the findings of this report.

BIBLIOGRAPHY

- de Jong, G. "The Undefiniteness in Kinematics for Friction Materials," pp. 55-70. Brussels Conference 58 on Earth Pressure Problems, vol. 1. Brussels: 1958.
- Dillon, H. B. "Structure and Identification of Clay Soils," Laboratory report for Soil Science 945, Michigan State University, East Lansing, Michigan, 1963.
- Haythornthwaite, R. M. "The Kinematics of Soils," pp. 235-250. Progress in Applied Mechanics, The Prager Anniversary Volume. U.S.A.: 1963.
- Haythornthwaite, R. M. "The Mechanics of the Triaxial Test for Soils." U.S. Army Ordnance Corps Tech. Rept. No. 1: 1959
- Holliday, Frank J. "Stress Transfer Due to Creep in a Saturated Clay." Master's thesis, Michigan State University, East Lansing, Michigan, 1963.
- Loh, A. K. "Mechanism of Friction and Cohesion in Clay." Ph.D. thesis, Michigan State University, East Lansing, Michigan, 1964.
- Rowe, P. W. "Importance of Free Ends in Triaxial Testing," pp. 1-27. Journal of the Soil Mechanics and Foundations Division, A.S.C.E., vol. 90. Ann Arbor: 1964.
- Schmertmann, John H. and Jorj O. Osterberg. "An Experimental Study of the Development of Cohesion and Friction with Axial Strain in Saturated Cohesive Soils," pp. 643-694. Research Conference on Shear Strength of Cohesive Soils, A.S.C.E. Ann Arbor: 1960.

APPENDIX A

SAMPLE DATA SHEETS AND STRESS-STRAIN
CURVES FOR UNCONFINED COMPRESSION TESTS

Table 10. Data sheet for W-K-U-1.

a. General Data		Water Content Data:	
Date - April 20, 1964		Container No.	319
Operator - Warder		Wt. of cont	26.97 g
Test - W-K-U-1		Wt. wet soil +	
Call - #3		cont.	63.73 g
Proving Ring - #3141		Wt. dry soil +	
Proving Ring Constant -		cont.	56.43 g
0.0382 kg/div		Wt. water	7.30 g
Length - 2.80 in = 7.11 cm		Dry wt.	29.46 g
Diameter = 3.33 cm		w	24.8 %
Area - 8.71 cm ²			
Vol. - 62.0 cm ³			
Weight of Sample - 120.00 g			
Strain Rate - 360 %/hr			
End Plates - conventional			

b. Stress-Strain Data

Load Dial	N	Axial Pressure KG/cm ²	Strain Dial	% Strain	Photograph Taken
0500	0	0	000	0	1
0643	143	0.619	050	1.79	
0795	295	1.25	100	3.57	2
0990	490	2.04	150	5.26	
1200	700	2.86	200	7.15	3
1425	925	3.71	250	8.93	
1604	1104	4.35	300	10.71	4
1800	1300	5.00	350	12.50	
1820	1320	4.98	400	14.38	5
1450	950	3.50	450	16.07	
1180	680	2.46	500	17.85	6

Table 11. Data sheet for W-K-U-6.

a. General Data	Wt. of sample	119.85
Date - May 3, 1964	Dry wt.	94.97
Operator - Warder	Wt. water	24.88
Test - W-K-U-6	w	26.2 %
Cell - #3		
Proving Ring - #684		
Proving Ring Const. - .147 kg/div.		
Length - 2.80 in = 7.11 cm		
Diameter - 3.33 cm		
Area - 8.71 cm ²		
Vol. - 62.0 cm ³		
Strain rate - 360 %/hr		
End Plates - frictionless		

b. Stress-Strain Data

Load Dial	N	Axial Pressure KG/cm ²	Strain Dial	% Strain	Photograph Taken
0000	0	0	000	0	6
0009	9	0.149	050	1.79	
0014	14	0.228	100	3.57	
0027	27	0.431	150	5.36	7
0047	47	0.737	200	7.15	
0077	77	1.185	250	8.94	
0112	112	1.69	300	10.71	8
0155	155	2.29	350	12.5	
0190	190	2.75	400	14.3	
0226	226	3.20	450	16.1	9
0259	259	3.59	500	17.9	
0280	280	3.81	550	19.6	
0293	293	3.90	600	21.4	10
0271	271	3.52	650	23.2	
0216	216	2.74	700	25.0	
0215	215	2.66	750	26.8	11

Table 12. Data sheet for W-S-U-4.

 a. General Data

Date - May 23, 1964
 Operator - Warder
 Test - W-S-U-4
 Cell - #3
 Proving ring - #314A
 Proving ring constant = 0.00455 kg/div.
 Length - 2.80 in = 7.11 cm
 Area - 10 cm²
 Vol. - 71.1
 Strain Rate - 400 %/hr
 End Plates - Conventional

Water Content Data:

Container no.	7
Container wt.	16.32 g
Cont. wt. + wet wt.	30.00 g
Cont. wt. + dry wt.	26.26 g
Water wt.	3.74 g
Dry wt.	9.94 g
w	37.7 %

Table 12. Continued.

Load Dial	N	Axial Pressure KG/cm ²	Strain Dial	% Strain
0500	0	0	000	0
0522	22	.098	050	1.79
0526	26	.114	100	3.57
0533	33	.142	150	5.36
0536-1/2	36-1/2	.154	200	7.15
0540	40	.166	250	8.94
0546	46	.187	300	10.71
0550	50	.199	350	12.50
0556	56	.218	400	14.3
0558-1/2	58-1/2	.223	450	16.1
0562	62	.232	500	17.9
--	--	--	550	19.6
0569	69	.247	600	21.4
0571-1/2	71-1/2	.250	650	23.2
0571	71	.242	700	25.0
0572-1/2	72-1/2	.242	750	26.8
0574	74	.240	800	28.6
0574	74	.234	850	30.4
0574	74	.228	900	32.1

Table 13. Data sheet for W-C-CU-2.

 a. General Data

Date - March 20, 1964
 Operator - Warder
 Test - W-C-CU-2
 Cell - #2
 Proving Ring - #3141
 Proving Ring Constant - .0382 kg/div
 Strain Rate - 4.7 %/hr
 End Plates - Conventional

Length - 2.64 in.
 Area - 8.88 cm²
 Volume - 59.5 cm³
 Initial wt. - 123.17 g
 Final wt. - 113.70 g

Initial Water Content Data:

Container no.	2
Container wt.	15.74
Cont. wt. + wet wt.	51.56
Cont. wt. + dry wt.	41.17
Water wt.	10.39
Dry wt.	25.43
w	40.8 %

Final Water Content Data:

	Top	Middle	Bottom
Container no.	3	4	10
Wet wt.	33.99 g	38.61 g	40.97 g
Dry wt.	26.10 g	29.41 g	30.87 g
Water wt.	7.89 g	9.20 g	10.10 g
w	30.1 %	31.3 %	32.8 %

Table 13. Continued.

b. Consolidation Data						
Date	Time	Elapsed Time -Min.	Chamber Pressure - KG/cm ²	Burette cc	Drainage cc	
3-21-64	8:53	0	2.00	0	0	
		.25	2.00	1.5	1.5	
		.5	2.00	1.7	1.7	
		8:54	1	2.00	2.0	2.0
		8:55	2	2.00	2.45	2.45
		8:58	5	2.00	3.40	3.40
		9:03	10	2.00	4.50	4.50
		9:08	15	2.00	5.50	5.50
		9:23	30	2.00	7.50 → 0	7.50
		9:53	60	2.00	2.30	9.80
		10:53	120	2.00	3.90	11.40
		12:53	240	2.00	4.45 → 0	11.95
		16:53	480	2.00	.35	12.30
3-22-64	08:53	1440	2.00	.60	12.55	

c. Stress-Strain Data

Time	Load Dial	N	Axial Pressure KG/cm ²	Strain Dial	% Strain	Photograph Taken
11:00	0500	0	0	000	0	9
11:15	0702	202	0.85	050	1.89	10
11:31	0743	243	1.01	100	3.79	11
11:59	0762-1/2	262-1/2	1.06	150	5.68	12
12:26	0774-1/2	274-1/2	1.09	200	7.58	13
12:54	0781	281	1.09	250	9.47	14
13:21	0784-1/2	284-1/2	1.07	300	11.38	15
14:15	0791	291	1.06	400	15.15	16

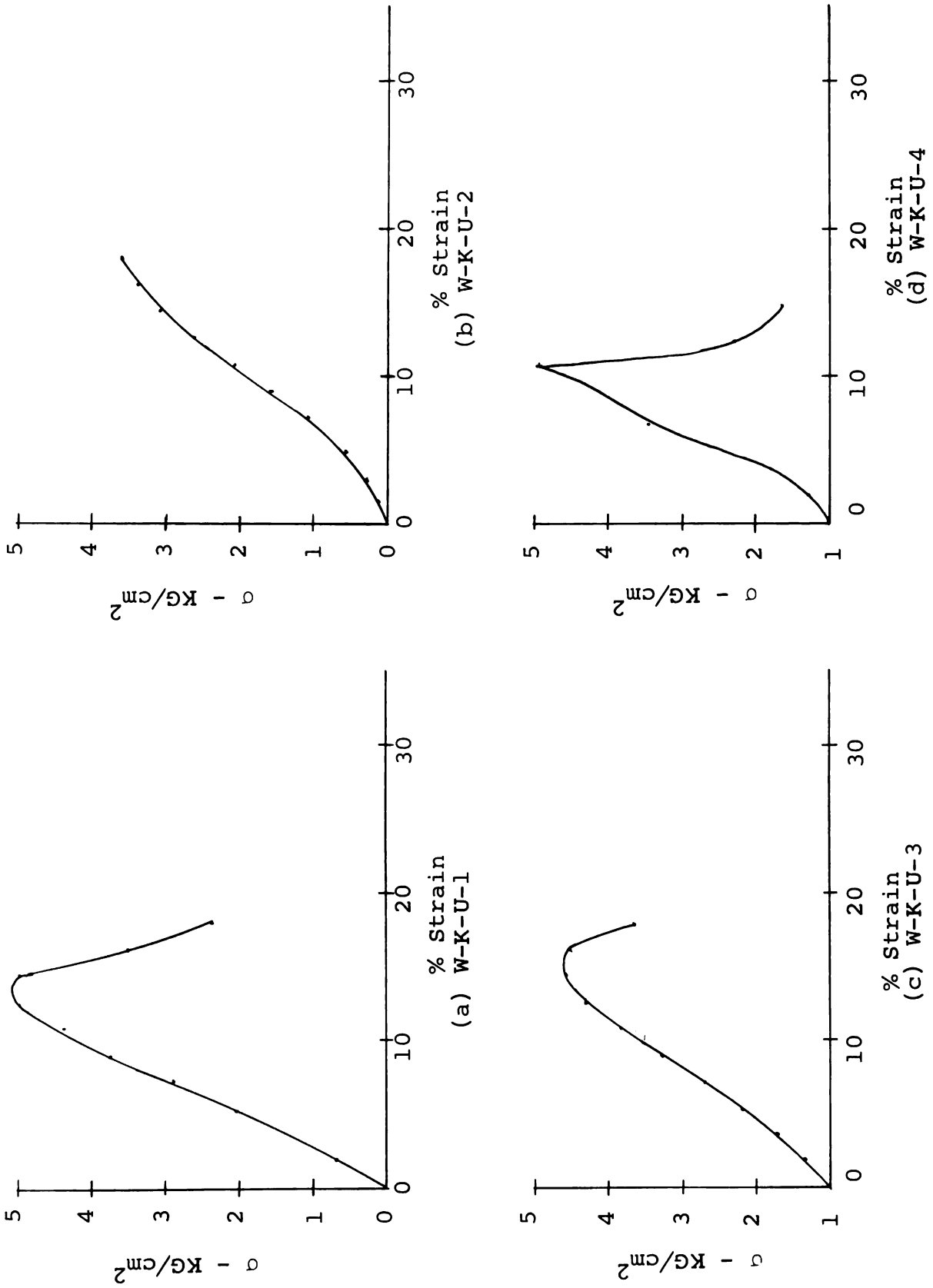


Fig. 14. Stress-strain curves for unconfined tests.

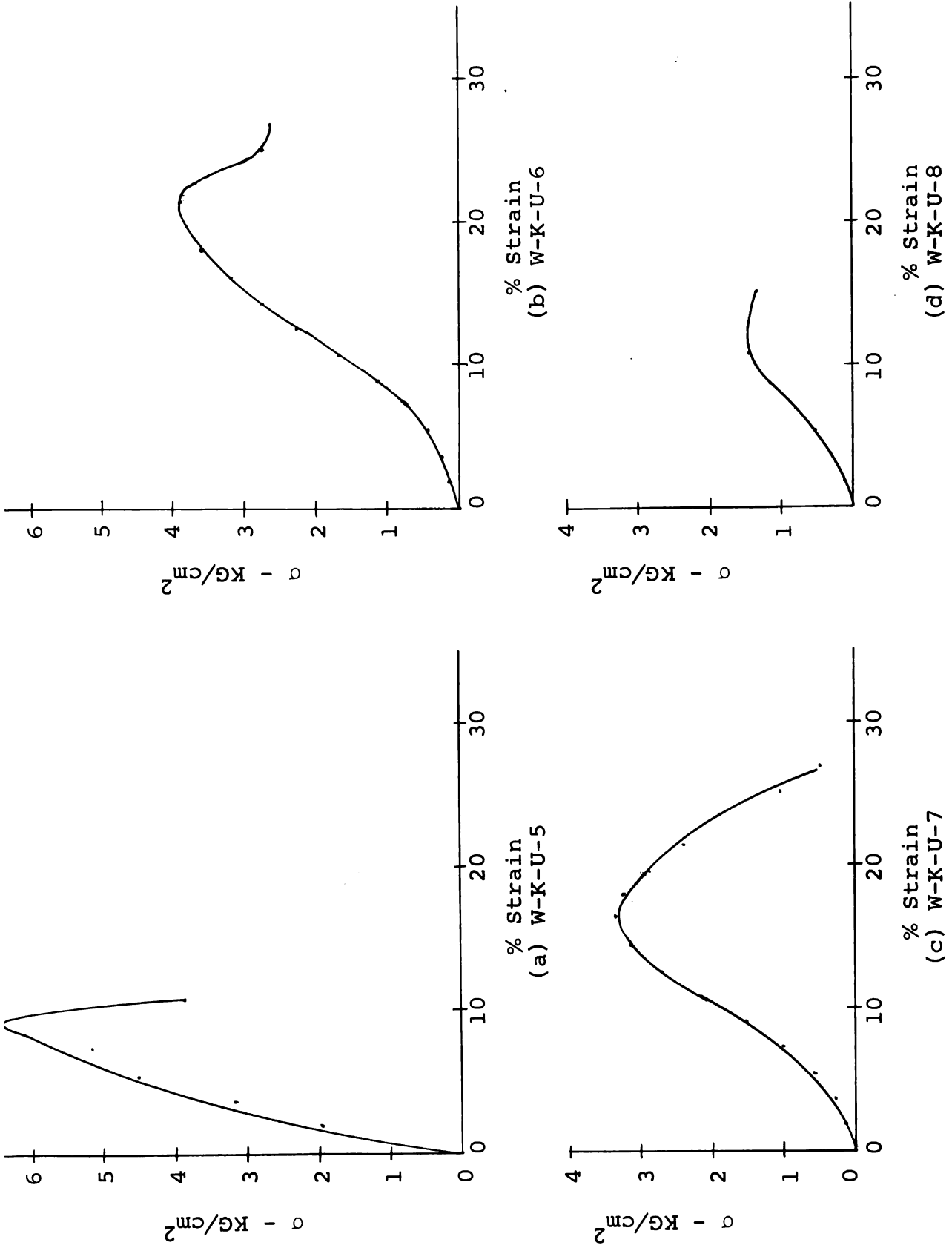


Fig. 15. Stress strain curves for unconfined tests.

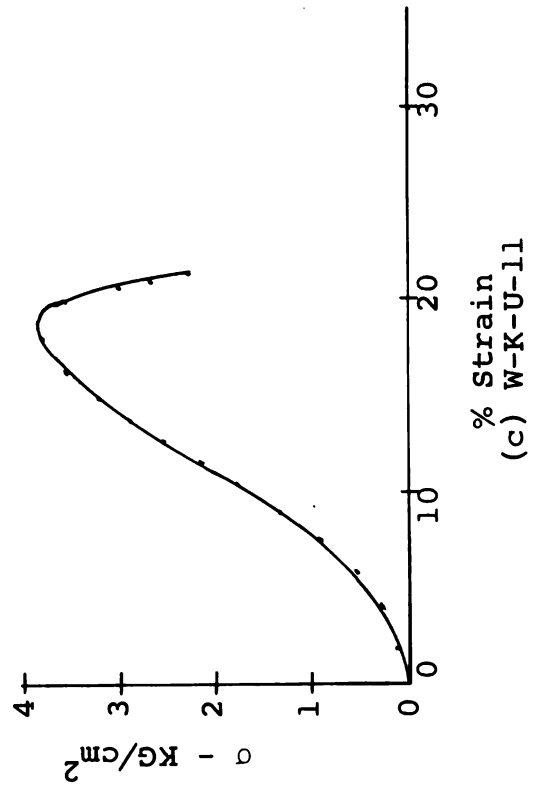
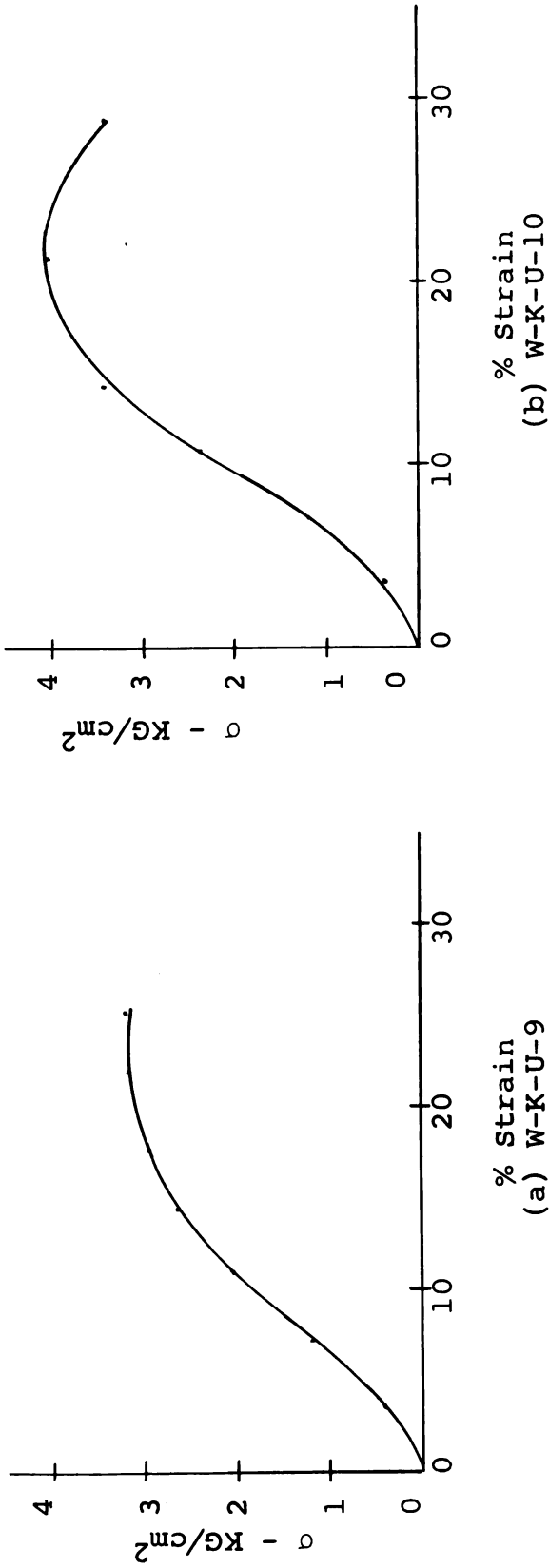


Fig. 16. Stress strain curves for unconfined compression tests.

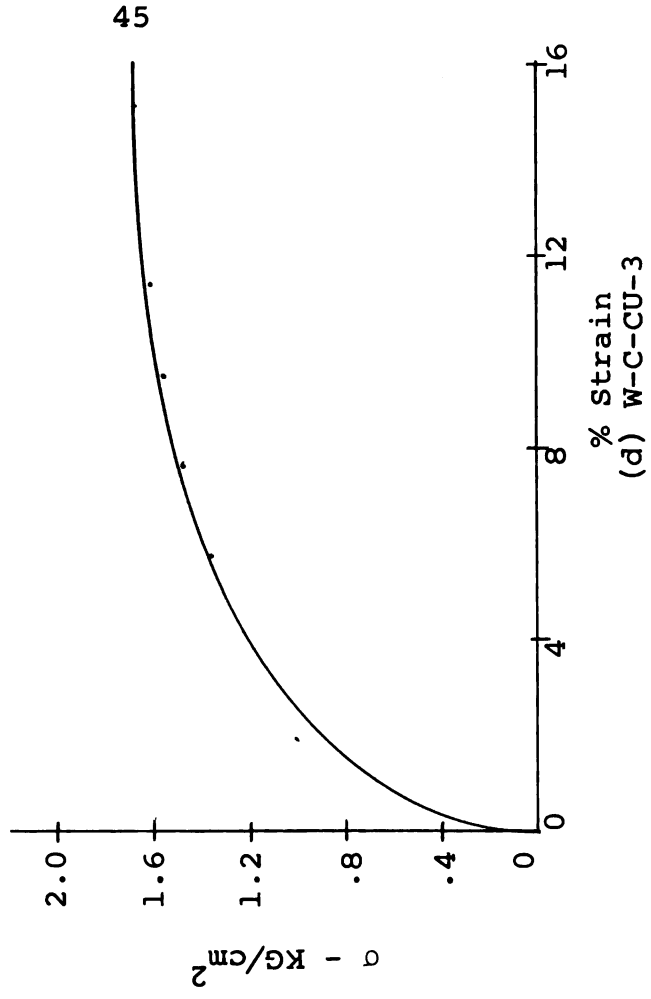
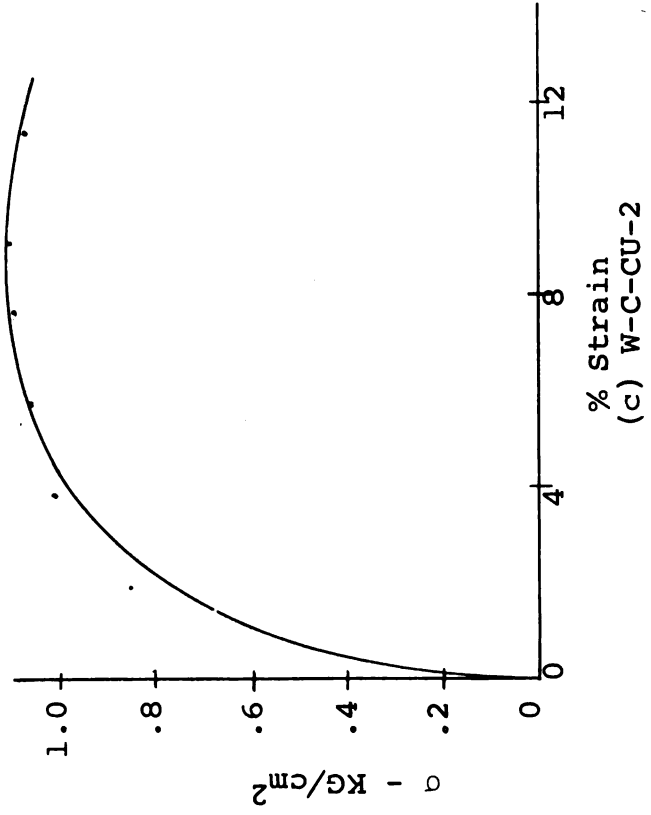
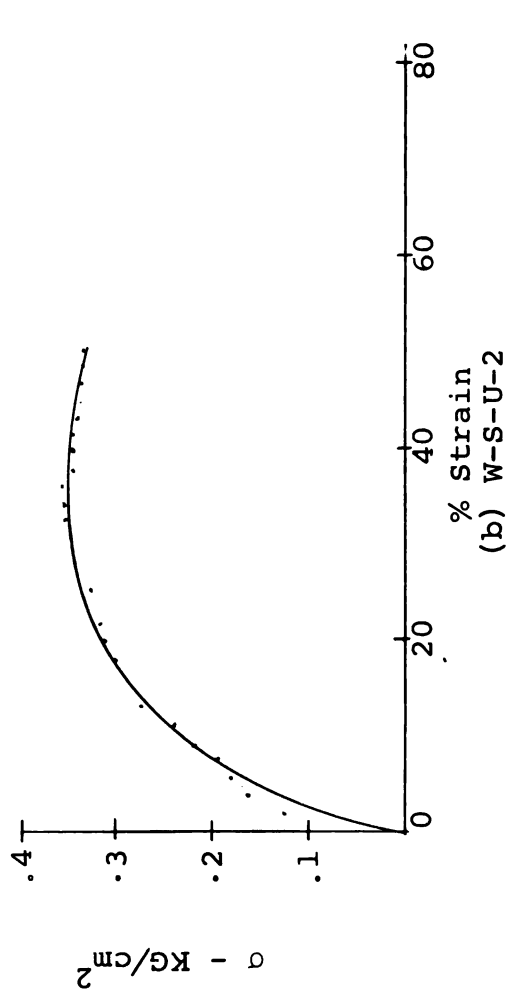
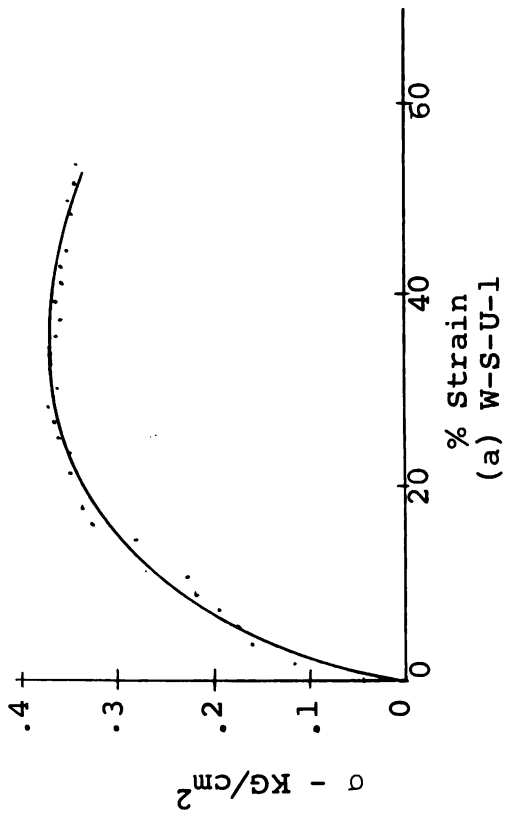


Fig. 17. Stress strain curves for unconfined tests.

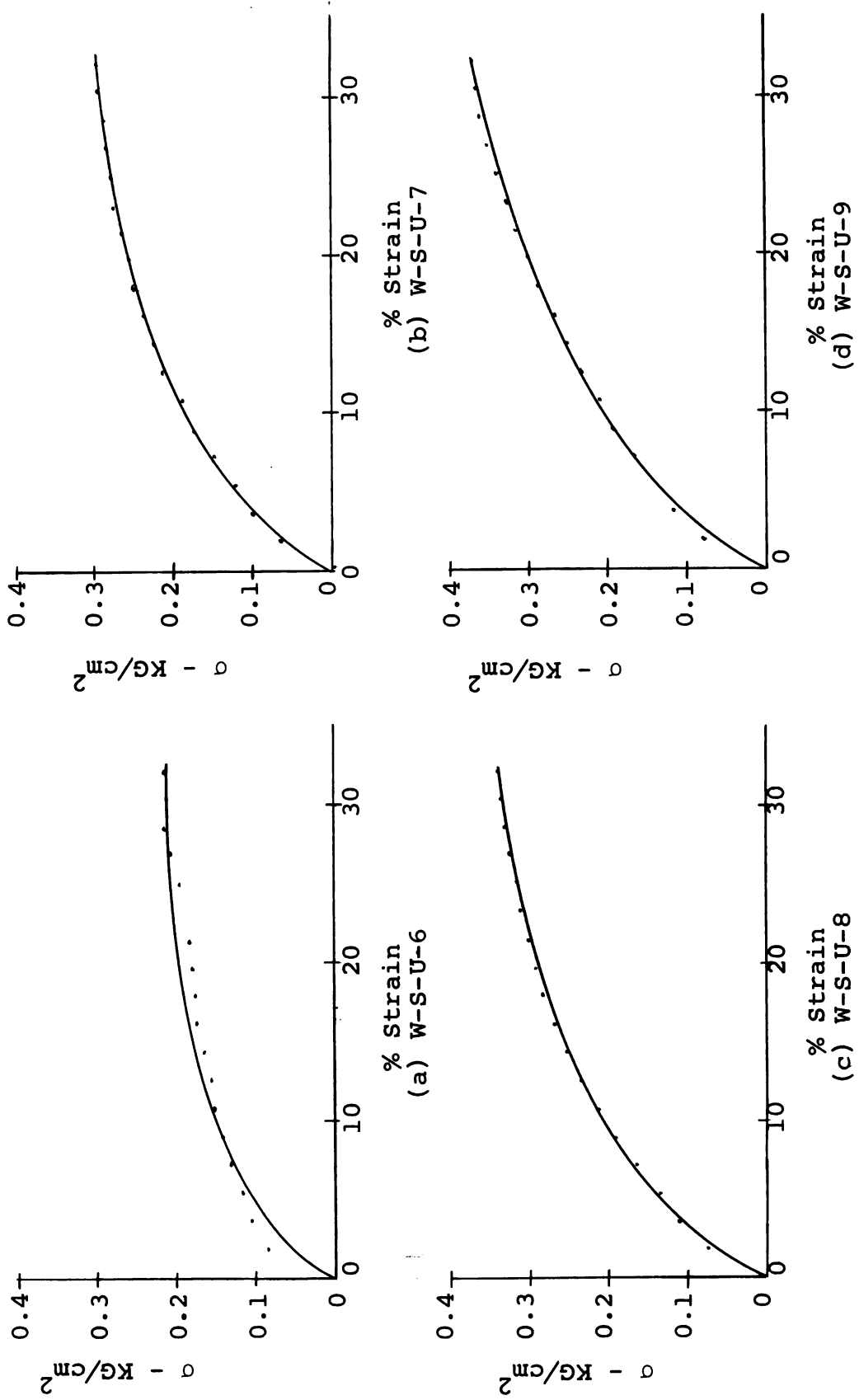


Fig. 18. Stress strain curves for unconfined tests.

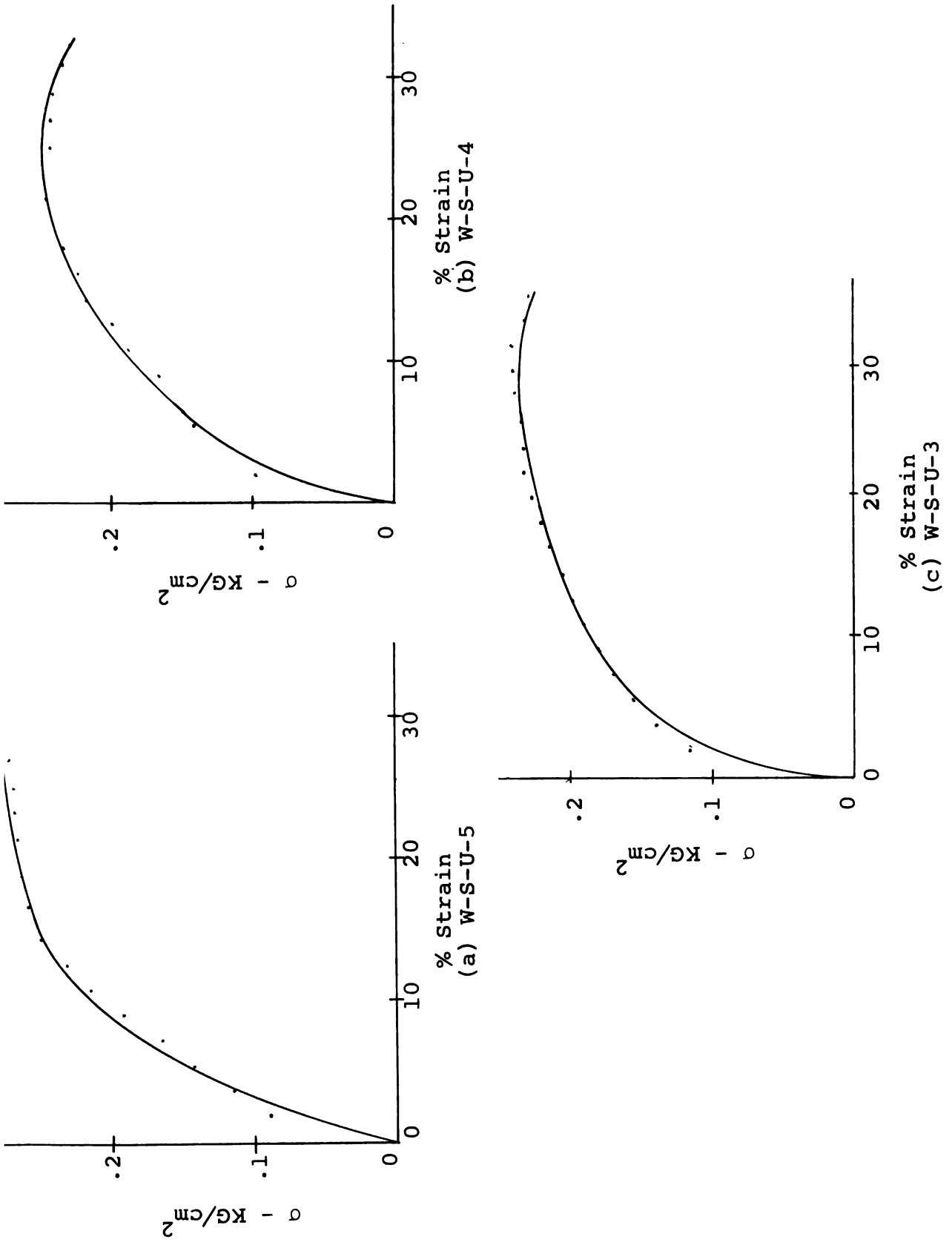


Fig. 19. Stress strain curves for unconfined tests.

APPENDIX B
SAMPLE DATA SHEETS AND CURVES
FOR CFS TESTS

Table 14. General data sheet for WF-CFS-6.

Date - July 13, 1964
Operator - Warder
Test - WF-CFS-6
Chamber Pressure - 2.00 kg/cm²
Cell - #4
Proving Ring - #3141
Proving Ring Const. - .0382 kg/div.
Strain Rate - 6.12 %/hr.
End Plates - Frictionless
Initial wt. - 127.01 g

Initial Measurements:

Length - 2.80 in.
Area - 10 cm²
Vol. - 71.1 cm³

After Consolidation:

Length - 2.64 in
Area - 8.93 cm²
Vol. - 59.8 cm³

Initial Water Content Data:

Container no.	2
Container wt.	15.74 g
Cont. wt. + wet wt.	49.07 g
Cont. wt. + dry wt.	39.06 g
Water wt.	10.01 g
Dry wt.	24.32 g
w	42.0 %

Final Water Content Data:

Final wet wt.	118.18 g
Final dry wt.	89.42 g
Water wt.	28.76 g
w	32.2 %

Table 15. Consolidation data sheet for WF-CFS-6.

Date	Time	Elapsed Time (min.)	Chamber Pressure (KG/cm ²)	Burette (cc)	Drainage (cc)	Pore Pressure (KG/cm ²)
7-14-64	07:58	0	2.00	0	0	--
		.25	2.00	1.70	1.70	
		.5	2.00	1.80	1.80	
	07:59	1	2.00	1.90	1.90	
	08:00	2	2.00	2.15	2.15	
	08:03	5	2.00	2.60	2.60	
	08:08	10	2.00	3.15	3.15	
	08:13	15	2.00	3.65	3.65	
	08:28	30	2.00	4.95	4.95	
	08:58	60	2.00	6.75 → 0	6.75	
	09:58	120	2.00	2.25	9.00	
	10:58	180	2.00	3.40	10.15	
	11:58	240	2.00	3.95 → 0	10.70	
	19:58	720	2.00	1.30	12.00	
7-15-64	08:06	1448	2.00	2.00	12.70	--
	08:15	--	4.00	Back Pressure Applied 2.00		

Table 16. Typical CFS data sheet from WF-CFS-6.

Time	Load Dial	N	Strain Dial	Strain %	Axial Pressure Δ_a -KG/cm ²	Pore Pressure Δ_u -KG/cm ²	Constant Pressure Cell
0903	988-1/2	288-1/2	110	4.17	1.187	1.187	2.50
0905	989	289	115	4.36	1.185	1.185	2.50
0906	990	290	120	4.55	1.187	1.187	2.50
0908	992-1/2	292-1/2	125	4.74	1.192	1.192	2.50
0910	993	293	130	4.93	1.192	1.192	2.50
0912	992	292	135	5.12	1.187	1.187	2.00
0915	999	299	140	5.31	1.212	1.212	2.00
0917	1004-1/2	304-1/2	145	5.50	1.231	1.231	2.00
0919	1007-1/2	307-1/2	150	5.69	1.24	1.24	2.00
0920	1010	310	155	5.88	1.25	1.25	2.00
0922	1014	314	160	6.07	1.26	1.26	2.00
0924	1018	318	165	6.26	1.275	1.275	2.00
0926	1022	322	170	6.45	1.29	1.29	2.00
0929	1025	325	175	6.64	1.299	1.299	2.00
0930	1029	329	180	6.82	1.312	1.312	2.00
0932	1033-1/2	333-1/2	185	7.01	1.327	1.327	2.00
0934	1038	338	190	7.20	1.341	1.341	2.00
--	--	--	195	7.39	--	--	2.00
0937	1045	345	200	7.58	1.363	1.363	2.00
0939	1048	348	205	7.77	1.373	1.373	2.00
0941	1052	352	210	7.95	1.388	1.388	2.00
0943	1055	1055	215	8.14	1.394	1.394	2.00

Table 17. CFS calculation sheet for WF-CFS-6.

Strain %	Upper Curve				Lower Curve			
	$\bar{\sigma}_1 = 2.00$				$\bar{\sigma}_1 = 1.50$			
	$\bar{\sigma}_1 - \bar{\sigma}_3$	$\bar{\sigma}_3$	$\frac{1}{2}(\frac{\bar{\sigma}_1}{\bar{\sigma}_3} - \frac{\bar{\sigma}_1}{\bar{\sigma}_3})$ Y_2	$\frac{1}{2}(\frac{\bar{\sigma}_1}{\bar{\sigma}_3} + \frac{\bar{\sigma}_1}{\bar{\sigma}_3})$ X_2	$\bar{\sigma}_1 - \bar{\sigma}_3$	$\bar{\sigma}_3$	$\frac{1}{2}(\frac{\bar{\sigma}_1}{\bar{\sigma}_3} - \frac{\bar{\sigma}_1}{\bar{\sigma}_3})$ Y_1	$\frac{1}{2}(\frac{\bar{\sigma}_1}{\bar{\sigma}_3} + \frac{\bar{\sigma}_1}{\bar{\sigma}_3})$ X_1
2.5	1.120	0.880	0.5600	1.4400	1.068	0.432	0.5340	0.9660
5.0	1.276	0.724	0.6380	1.3620	1.192	0.308	0.5960	0.9040
7.5	1.378	0.622	0.6890	1.3110	1.280	0.220	0.6400	0.8600
10.0	1.433	0.567	0.7165	1.2835	1.330	0.170	0.6650	0.8350
12.5	1.463	0.547	0.7265	1.2735	1.348	0.152	0.6740	0.8260
15.0	1.440	0.560	0.7200	1.2800	1.329	0.171	0.6645	0.8356
17.5	1.387	0.613	0.6935	1.3065	1.258	0.242	0.6290	0.8710
20.0	1.338	0.662	0.6690	1.3310	1.207	0.293	0.6035	0.8965
22.5	1.301	0.699	0.6505	1.3495	1.777	0.323	0.5885	0.9115
25.0	1.280	0.720	0.6400	1.3600	1.155	0.345	0.5775	0.9225
27.5	1.268	0.732	0.6340	1.3660	1.143	0.351	0.5715	0.9285
30.0	1.261	0.739	0.6305	1.3695	1.140	0.360	0.5700	0.9300
32.5	1.259	0.741	0.6295	1.3705	1.137	0.363	0.5685	0.9315
35.0	1.256	0.744	0.6280	1.3720	1.133	0.367	0.5665	0.9335
37.5	1.254	0.746	0.6270	1.3730	1.132	0.368	0.5660	0.9340
40.0	1.255	0.745	0.6275	1.3725	1.131	0.369	0.5655	0.9345

Test No. WF-CFS-6

Sample No. WC-16

Computed by Warder

Date 7-17-64

$Y_2 - Y_1$	$X_2 - X_1$	$\text{Tan } \alpha$ $= \text{Sin } \phi_\epsilon$	ϕ_ϵ	$X_1 \text{Tan } \alpha$	$\frac{Y_1 - X_1 \text{Tan } \alpha}{a}$ $= C_\epsilon \cos \phi_\epsilon$	C_ϵ
.0260	.474	.055	3.15 ^o	.0531	.4809	.482
.0420	.458	.0917	5.26 ^o	.0829	.5131	.515
.0490	.451	.1087	6.24 ^o	.0935	.4565	.551
.0515	.4485	.115	6.60 ^o	.0960	.5690	.572
.0525	.4475	.1172	6.73 ^o	.0968	.5772	.582
.0555	.4445	.125	7.18 ^o	.1044	.5601	.565
.0645	.4355	.148	8.50 ^o	.1289	.5001	.505
.0655	.4345	.151	8.68 ^o	.1354	.4681	.473
.0620	.438	.1418	8.15 ^o	.1293	.4592	.464
.0625	.4375	.143	8.22 ^o	.1319	.4456	.451
.0625	.4375	.141	8.22 ^o	.1328	.4387	.444
.0605	.4395	.1377	7.90 ^o	.1281	.4419	.447
.0610	.4390	.139	8.00 ^o	.1295	.4390	.444
.0615	.4385	.1403	8.07 ^o	.1310	.4355	.441
.0610	.4390	.139	8.00 ^o	.1298	.4362	.441
.0620	.4380	.1417	8.14 ^o	.1324	.4331	.438

Table 18. General data sheet for GF-CFS-2

Date - August 10, 1964
 Operator - Warder
 Test - GF-CFS-2
 Chamber Pressure - 2.00 kg/cm²
 Cell - #4
 Proving Ring - #3141
 Proving Ring Const. - .0382 kg/div.
 Strain Rate - 1.24 %/hr.
 End Plates - Frictionless
 Initial wt. - 126.03

Initial Measurements:

Length	2.80 in
Area	10 cm ²
Vol.	71.1 cm ³

After Consolidation:

Length	2.66 in.
Area	9.09 cm ²
Vol.	61.4 cm ³

Initial Water Content Data:

Container no.	3
Container wt.	15.76 g
Cont. wt. + wet wt.	47.00 g
Cont. wt. + dry wt.	37.95 g
Water wt.	9.05 g
Dry wt.	22.19 g
w	40.8 %

Final Water Content Data:

Final wet wt.	116.95 g
Final dry wt.	88.29 g
Water wt.	28.66 g
w	32.5 %

Table 19. Consolidation data sheet for GF-CFS-2.

Date	Time	Elapsed Time (min.)	Chamber Pressure (KG/cm ²)	Burette Drainage (cc)	Drainage (cc)	Pore Pressure (KG/cm ²)
8-11-64	07:52	0	2.00	0	0	--
		.25	2.00	1.50	1.50	
		.5	2.00	1.90	1.90	
	07:53	1	2.00	2.05	2.05	
	07:54	2	2.00	2.30	2.30	
	07:57	5	2.00	2.80	2.80	
	08:02	10	2.00	3.30	3.30	
	08:07	15	2.00	3.70	3.70	
	08:22	30	2.00	4.70	4.70	
	08:52	60	2.00	6.10	6.10	
	09:52	120	2.00	7.80	7.85	
	10:52	180	2.00	.95	8.80	
	12:02	250	2.00	1.60	9.45	
	14:00	368	2.00	2.35	10.20	
	15:52	480	2.00	2.80	10.65	
19:52	720	2.00	3.25	11.10		
8-12-64	07:52	1440	2.00	3.75	11.60	--
	08:00	--	4.00	Back Pressure Applied 2.00		

Table 20. Typical CFS data sheet from GF-CFS-2.

Time	Load Dial	N	Strain Dial	Strain %	Axial Pressure Δ_a -KG/cm ²	Pore Pressure Δ_u -KG/cm ²	Constant Pressure Cell
1130	872-1/2	272-1/2	090	3.38	1.108	1.108	2.00
1138	876	276	094	3.53	1.12	1.12	2.00
1145	879-1/2	279-1/2	098	3.68	1.131	1.131	2.00
1152	883	283	102	3.83	1.143	1.143	2.00
1200	886	286	106	2.98	1.152	1.152	2.00
1206	888-1/2	288-1/2	110	4.14	1.161	1.161	2.00
1214	891	291	114	4.29	1.17	1.17	2.00
1222	893-1/2	293-1/2	118	4.44	1.18	1.18	2.00
1229	895-1/2	295-1/2	122	4.59	1.185	1.185	2.00
1236	898	298	126	4.74	1.192	1.192	2.00
1244	900-1/2	300-1/2	130	4.89	1.202	1.202	2.50
1251	902	302	134	5.04	1.204	1.204	2.50
1259	903	303	138	5.19	1.206	1.206	2.50
1306	902	302	142	5.34	1.201	1.201	2.50
1314	901	301	146	5.49	1.195	1.195	2.50
1321	899	299	150	5.65	1.185	1.185	2.50
1330	900-1/2	300-1/2	154	5.80	1.189	1.189	2.50
1338	901-1/2	301-1/2	158	5.95	1.19	1.19	2.50
1345	899	299	162	6.10	1.18	1.18	2.00
1353	903	303	166	6.25	1.193	1.193	2.00
1400	907	307	170	6.40	1.209	1.209	2.00
1408	909-1/2	309-1/2	174	6.55	1.215	1.215	2.00

Table 21. CFS calculation sheet for GF-CFS-2.

Strain %	Upper Curve				Lower Curve			
	$\bar{\sigma}_1 = 2.00$				$\bar{\sigma}_1 = 1.50$			
	$\bar{\sigma}_1 - \bar{\sigma}_3$	$\bar{\sigma}_3$	$\frac{1}{2}(\frac{\bar{\sigma}_1}{\bar{\sigma}_3} - \frac{\bar{\sigma}_1}{\bar{\sigma}_3})$ Y_2	$\frac{1}{2}(\frac{\bar{\sigma}_1}{\bar{\sigma}_3} - \frac{\bar{\sigma}_1}{\bar{\sigma}_3})$ X_2	$\bar{\sigma}_1 - \bar{\sigma}_3$	$\bar{\sigma}_3$	$\frac{1}{2}(\frac{\bar{\sigma}_1}{\bar{\sigma}_3} - \frac{\bar{\sigma}_1}{\bar{\sigma}_3})$ Y_1	$\frac{1}{2}(\frac{\bar{\sigma}_1}{\bar{\sigma}_3} - \frac{\bar{\sigma}_1}{\bar{\sigma}_3})$ X_1
2.50	1.051	.949	.5255	1.4745	1.032	.468	.5160	.9840
3.75	1.139	.861	.5695	1.4305	1.109	.391	.5545	.9455
5.00	1.197	.803	.5985	1.4015	1.159	.341	.5795	.9205
6.25	1.238	.762	.6190	1.3810	1.193	.307	.5965	.9035
7.50	1.267	.733	.6335	1.3665	1.217	.283	.6085	.8915
8.75	1.283	.717	.6415	1.3585	1.228	.272	.6140	.8860
10.00	1.292	.708	.6460	1.3540	1.231	.269	.6155	.8845
12.50	1.289	.711	.6445	1.3555	1.219	.281	.6095	.8205
15.00	1.263	.737	.6315	1.3685	1.180	.320	.5900	.9100
17.50	1.230	.770	.6150	1.3850	1.142	.358	.5710	.9290
20.00	1.201	.799	.6005	1.3995	1.112	.388	.5560	.9440
25	1.160	.840	.5800	1.4200	1.069	.431	.5345	.9655
30	1.132	.868	.5660	1.4340	1.039	.461	.5195	.9805
35	1.111	.889	.5555	1.4445	1.017	.483	.5085	.9915
40	1.094	.906	.4570	1.4530	1.000	.500	.5000	1.000

Test No. GF-CFS-2
 Computed by Warder

Sample No. G-16
 Date 9-9-64

$Y_2 - Y_1$	$X_2 - X_1$	$\text{Tan } \alpha$ $= \text{Sin } \phi_\epsilon$	ϕ_ϵ	$X_1 \text{Tan } \alpha$	$Y_1 - X_1 \text{Tan } \alpha$ $= a$ $= C_\epsilon \cos \phi_\epsilon$	C_ϵ
.0095	.4905	.0194	1.11 ^o	.0191	.4969	.497
.0150	.4850	.0309	1.77 ^o	.0292	.5253	.526
.0190	.4810	.0395	2.26 ^o	.0364	.5431	.544
.0225	.4775	.0471	2.70 ^o	.0426	.5539	.555
.0250	.4750	.0526	3.02 ^o	.0469	.5616	.563
.0275	.4725	.0582	3.34 ^o	.0516	.5624	.564
.0305	.4695	.0650	3.73 ^o	.0575	.5580	.559
.0350	.4650	.0753	4.32 ^o	.0671	.5424	.544
.0415	.4585	.0905	5.20 ^o	.0824	.5076	.509
.0440	.4560	.0965	5.54 ^o	.0896	.4814	.483
.0445	.4555	.0977	5.62 ^o	.0922	.4638	.466
.0455	.4545	.1001	5.75 ^o	.0966	.4379	.440
.0465	.4535	.1025	5.88 ^o	.1005	.4190	.421
.0470	.4530	.1038	5.95 ^o	.1029	.4056	.408
.0470	.4530	.1038	5.95 ^o	.1038	.3962	.399

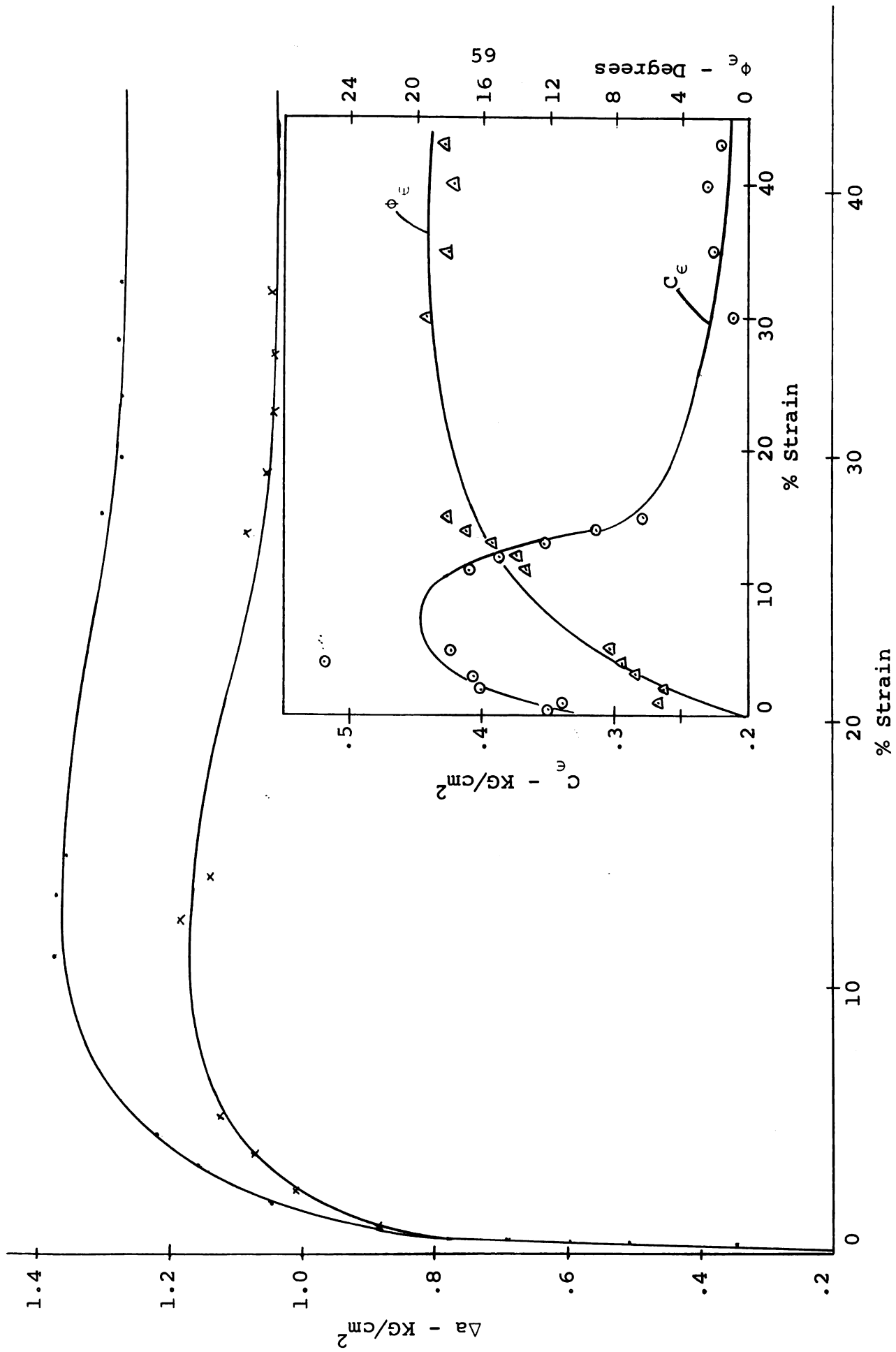


Fig. 20. CFS curves for W-F-CFS-2

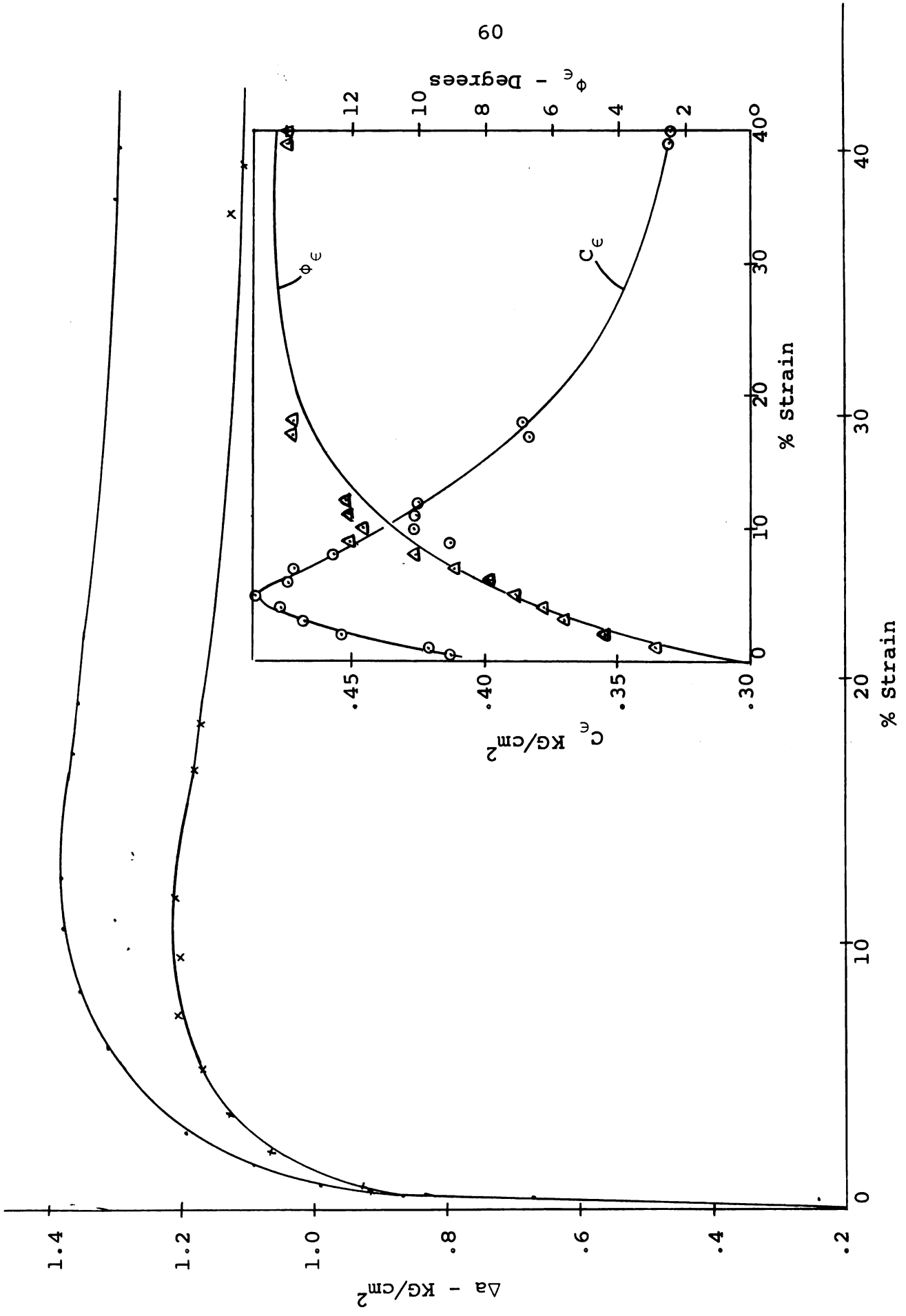


Fig. 21. CFS curves for W-F-CFS-3.

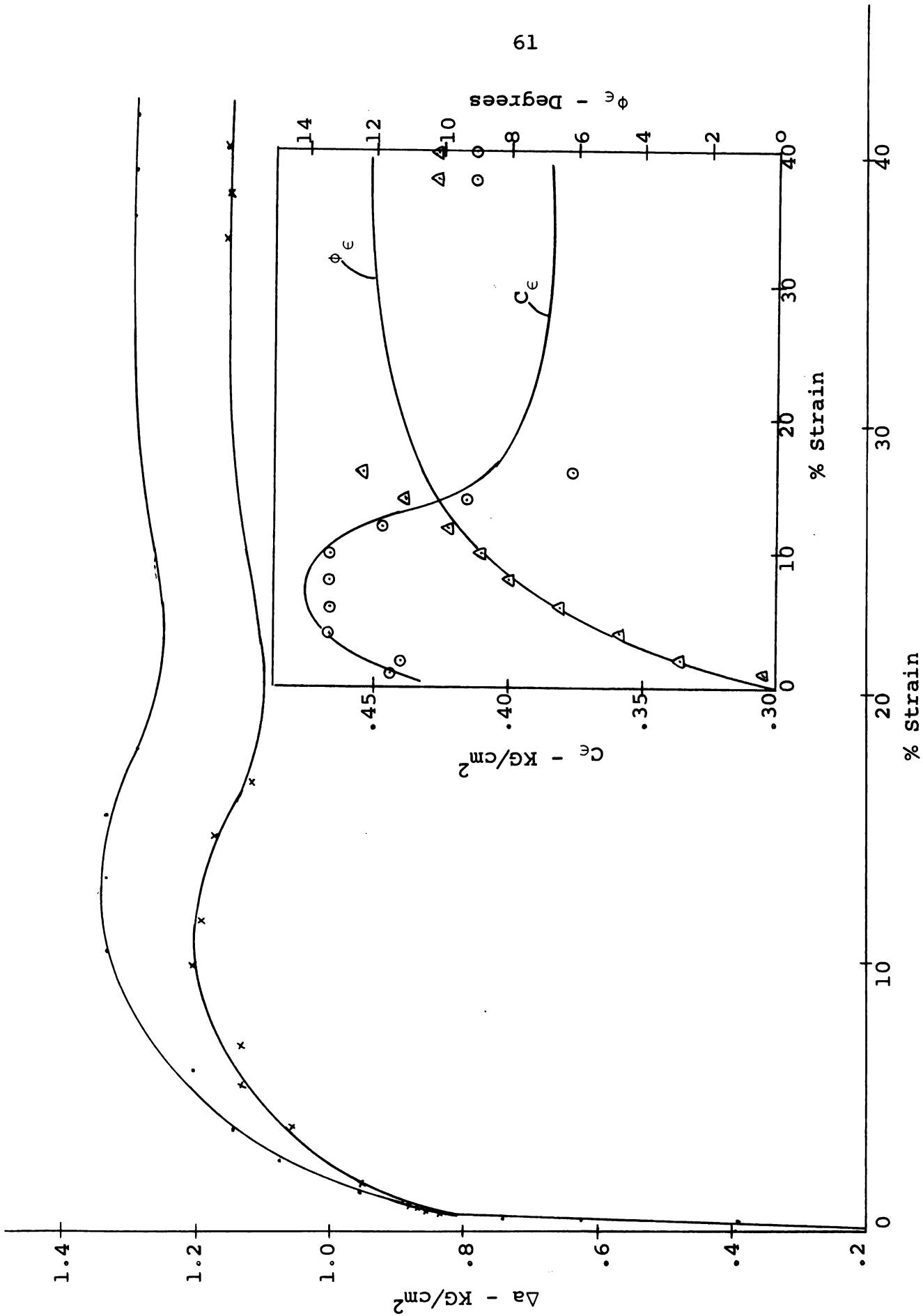


Fig. 22. CFS curves for W-F-CFS-4.

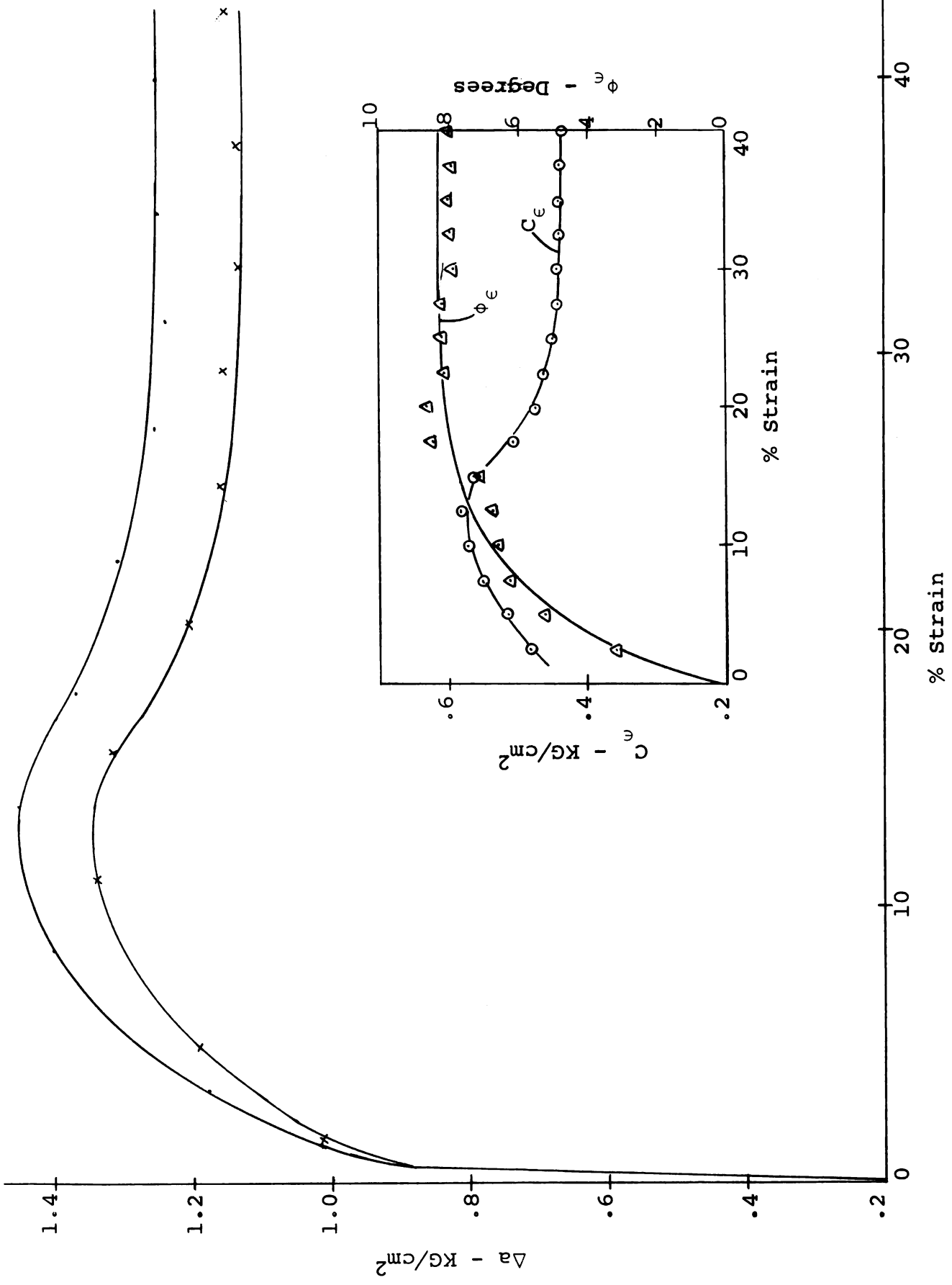


Fig. 23. CFS curves for WF-CFS-6.

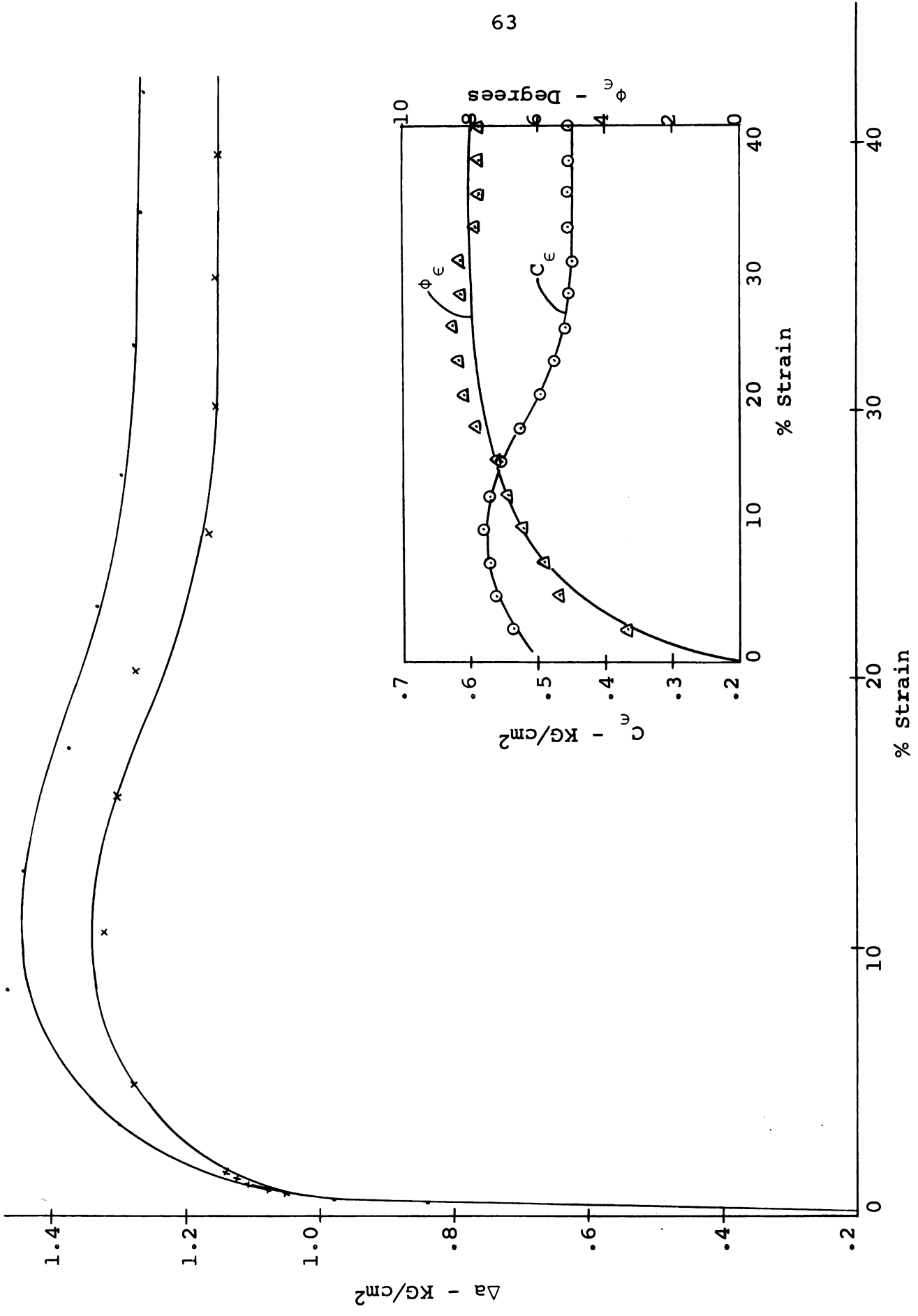


Fig. 24. CFS curves for WF-CFS-7.

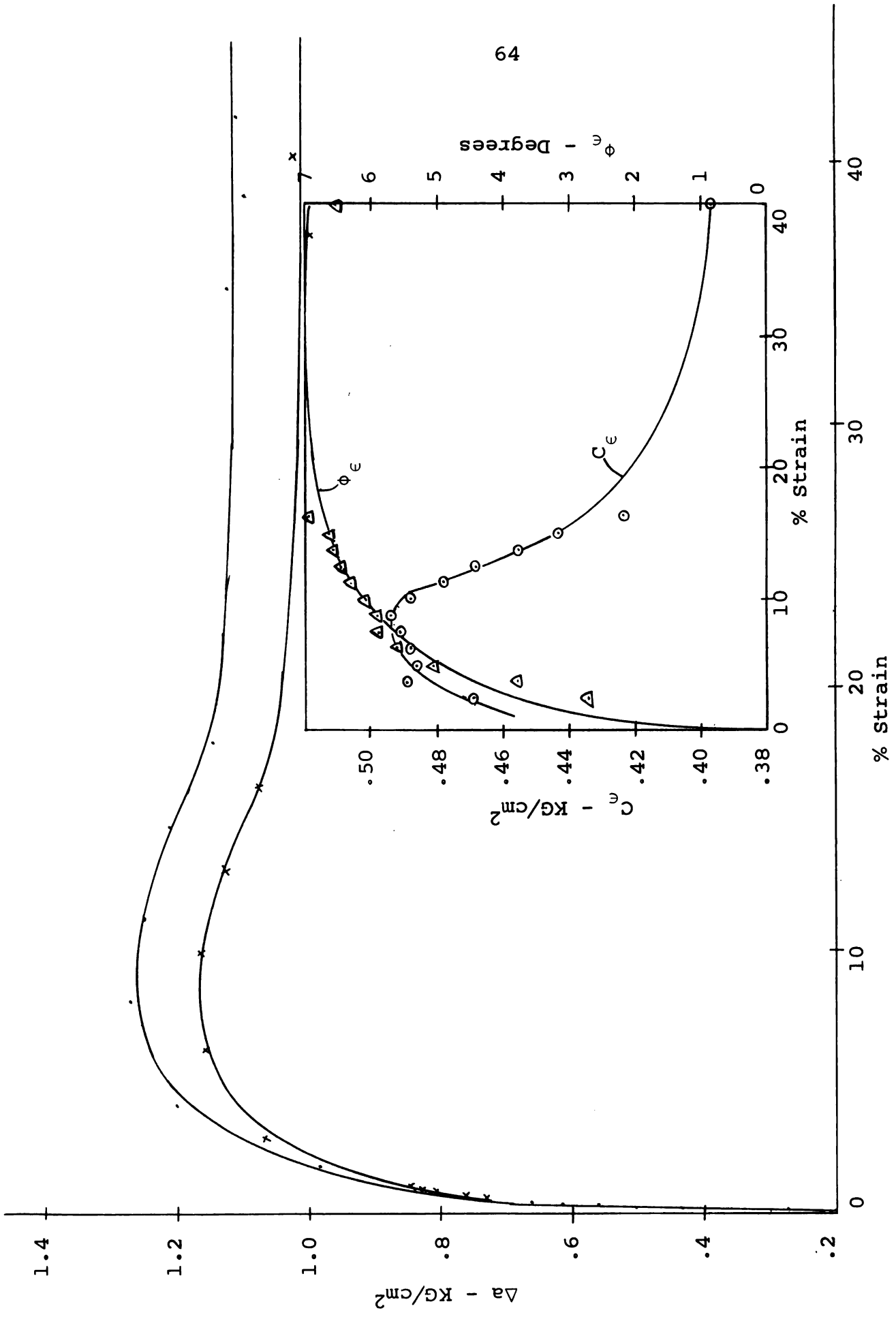


Fig. 25. CFS curves for GF-CFS-1.

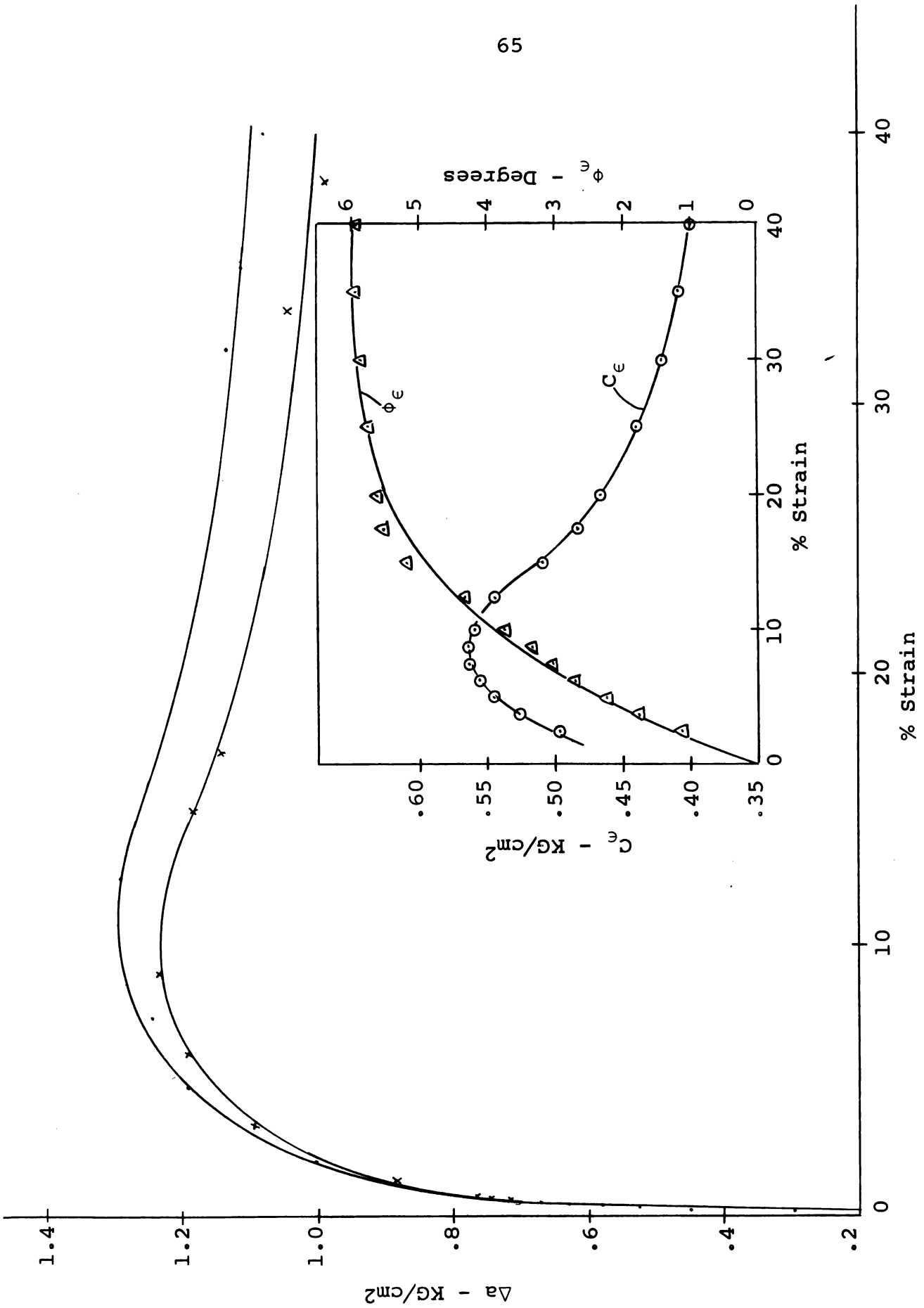


Fig. 26. CFS curves for GF-CFS-2.

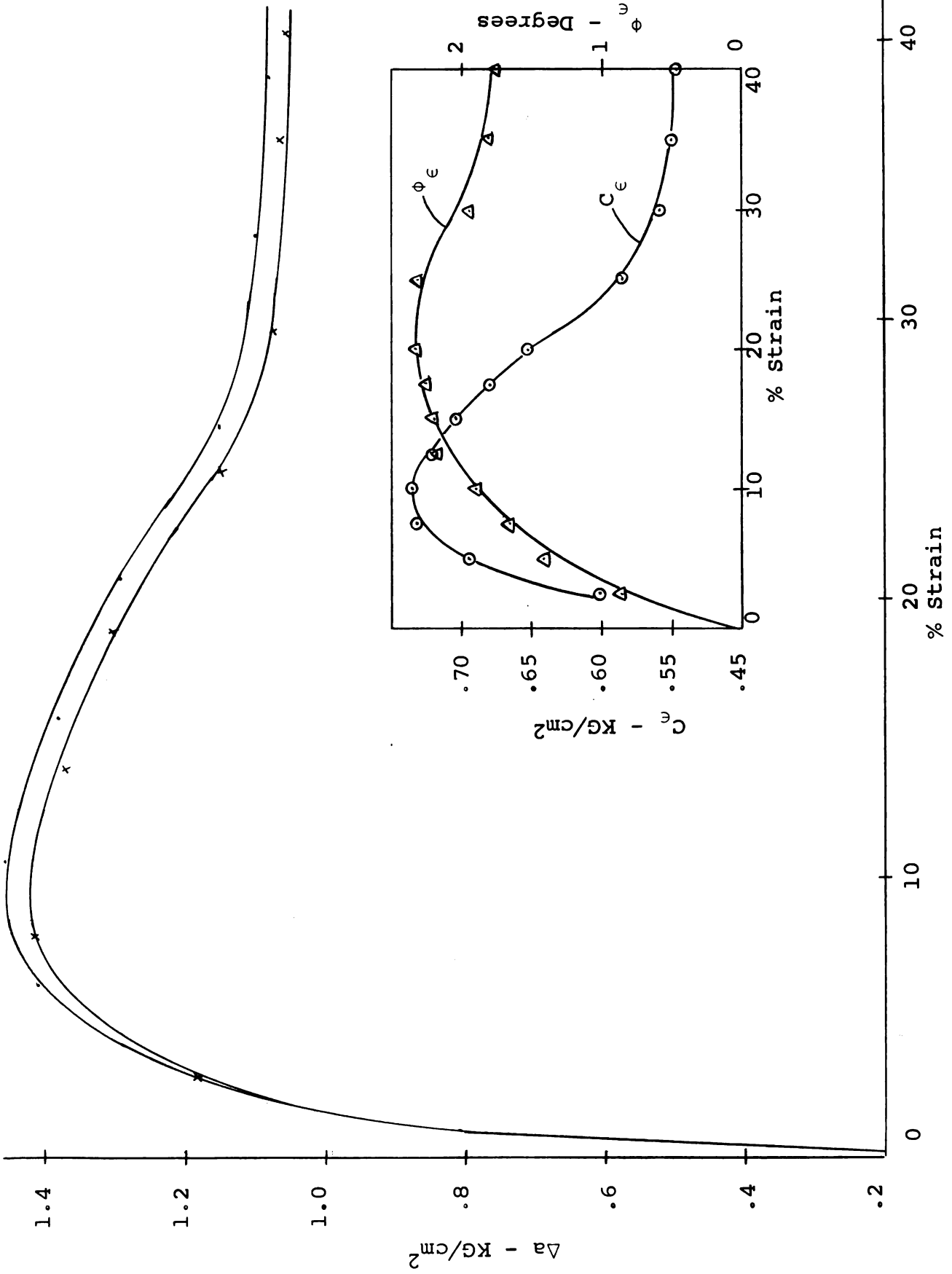


Fig. 27. CFS curves for GF-CFS-3.

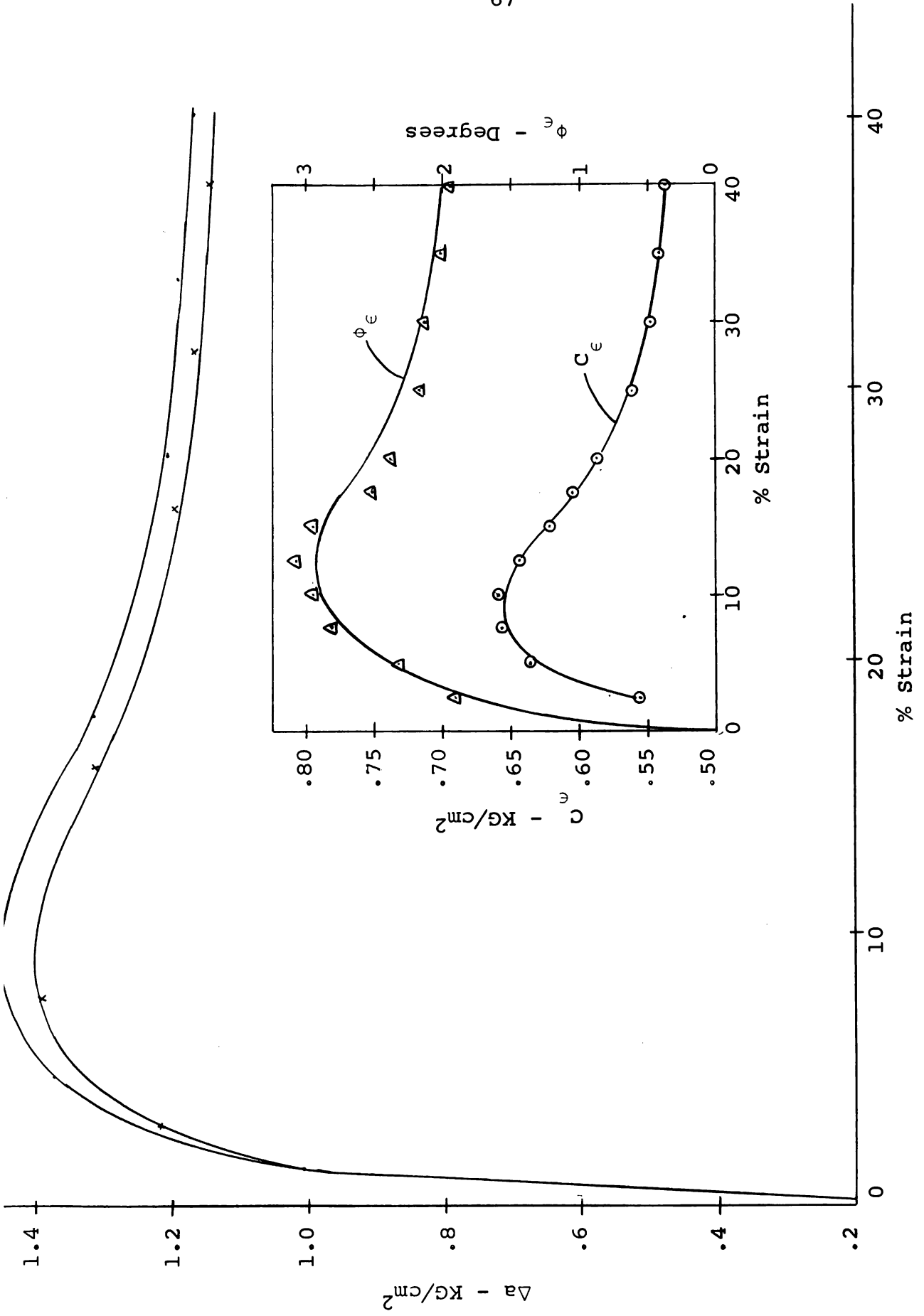


Fig. 28. CFS curves for GF-CFS-4.

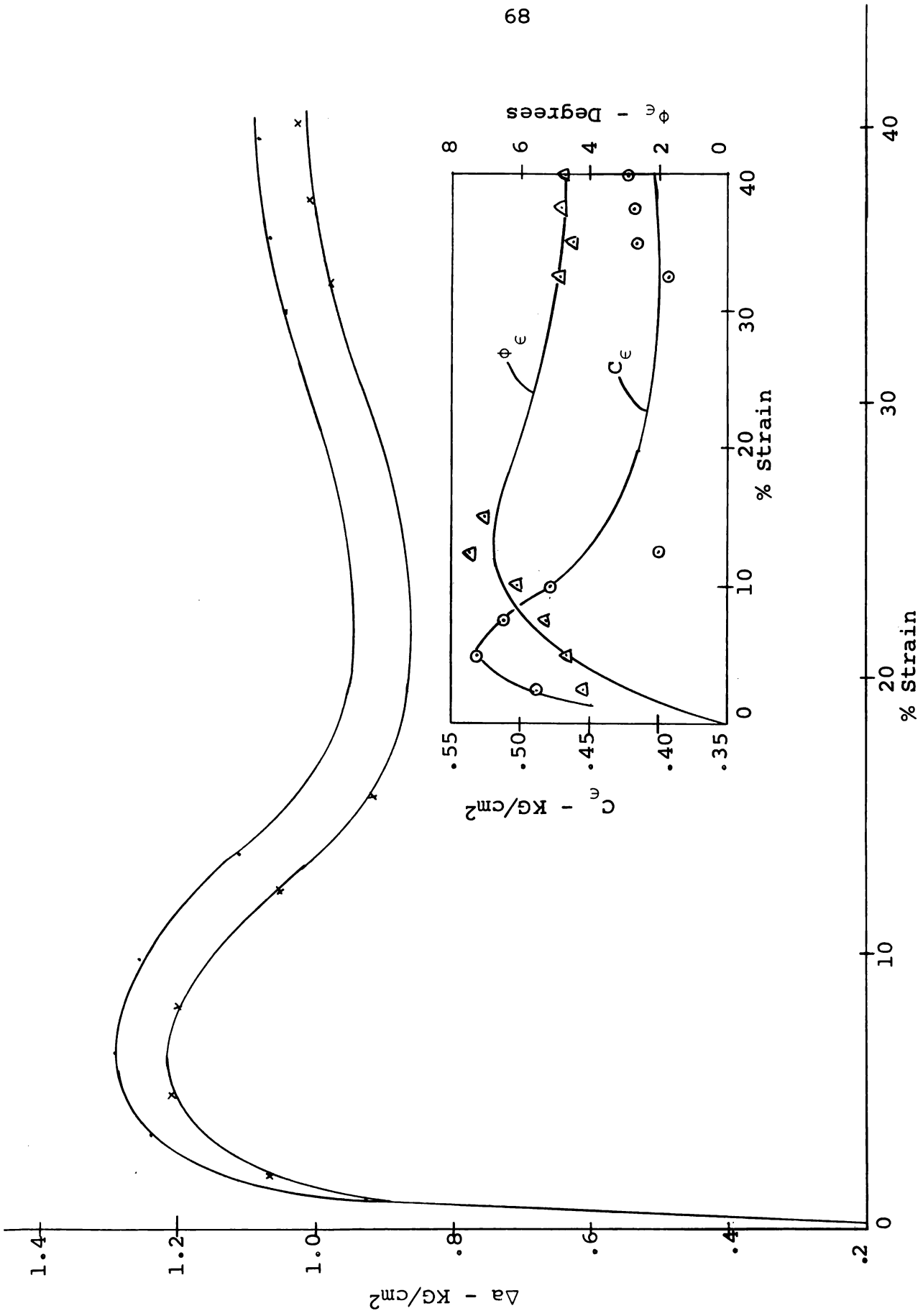


Fig. 29. CFS curves for GF-CFS-5.

APPENDIX C

**SAMPLE CALCULATIONS AND INTERPRETATION
OF DATA**

1. Sample Calculations

(a) Calculation of stress

The stress is calculated on the assumption that the area increases as the inverse of one minus the axial strain. The load is determined from a linearly elastic proving ring which is calibrated and the constant slope of the load-deflection curve is known. An example is given from WF-CFS-6.

Given:

No. of divisions on load dial = $N = 345$ div.

Proving ring constant = $C = 0.0382$ kg/div.

Strain = $\epsilon = 7.58\% = .0758$ in/in.

Area of start of test = $A_0 = 8.93$ cm²

Stress calculation:

$$\begin{aligned} \text{Deviation Stress} = \Delta a &= \frac{CN(1-\epsilon)}{A_0} \\ &= \frac{(.0382)(345)(1-.0758)}{8.93} \\ &= 1.363 \text{ kg/cm}^2 \end{aligned}$$

(b) Corrected dimensions after consolidation

If the sample is consolidated before the test is run, it is necessary to correct the dimension of the sample to account for changes due to consolidation. This is done on the assumption that the area changes as the two-thirds power of the ratio of the volume at the end of consolidation

to the original volume and the length varies as the one-third power of this ratio. The volume change is measured by means of a burette during consolidation. An example from test WF-CFS-6 is given below.

Given:

$$\text{Original volume} = V = 71.1 \text{ cm}^3$$

$$\text{Original area} = A = 10 \text{ cm}^2$$

$$\text{Original length} = L = 2.80 \text{ in}$$

$$\text{Volume change during consolidation} = \Delta V = 11.1 \text{ cm}^3$$

Calculation of corrected dimensions:

$$\text{Corrected volume} = V_o = V - \Delta V = 71.1 - 11.1 = 60.0 \text{ cm}^3$$

$$\frac{V_o}{V} = \frac{60.0}{71.1} = 0.844$$

$$\text{Corrected area} = A_o = A \left(\frac{V_o}{V}\right)^{2/3} = 10(.844)^{2/3} = 8.93 \text{ cm}^2$$

$$\text{Corrected length} = L_o = L \left(\frac{V_o}{V}\right)^{1/3} = 2.80(.844)^{1/3} = 2.64 \text{ in}$$

(c) CFS calculations

Examples of calculating C_ϵ and ϕ_ϵ from a CFS test are given in Tables 17 and 21. These calculations are based on the geometry of two Mohr circles, one representing the upper curve and one representing the lower curve. For a detailed explanation see Holliday (1963).

$\bar{\sigma}_1$ is constant for each curve throughout the test since the porewater pressure is continuously adjusted to balance the increase in axial pressure. $(\bar{\sigma}_1 - \bar{\sigma}_3)$ is the deviation stress and is calculated as shown in part (a) of this appendix. The remaining calculations in Tables 17 and 21 are self-explanatory.

2. Interpretation of Data

The failure stress and strain correspond to the peak on the stress-strain curve. In cases where the stress-strain curve did not reach a peak, the values of stress and strain at the end of the test were recorded. In the two unconfined compression tests in which the instantaneous load was applied, the failure strain was estimated on the basis of the final deformation. The peak deviator stress referred to in Tables 8 and 9 refers to the upper curve in the CFS test.

APPENDIX D

PHOTOGRAPHS OF DEFORMED SPECIMENS

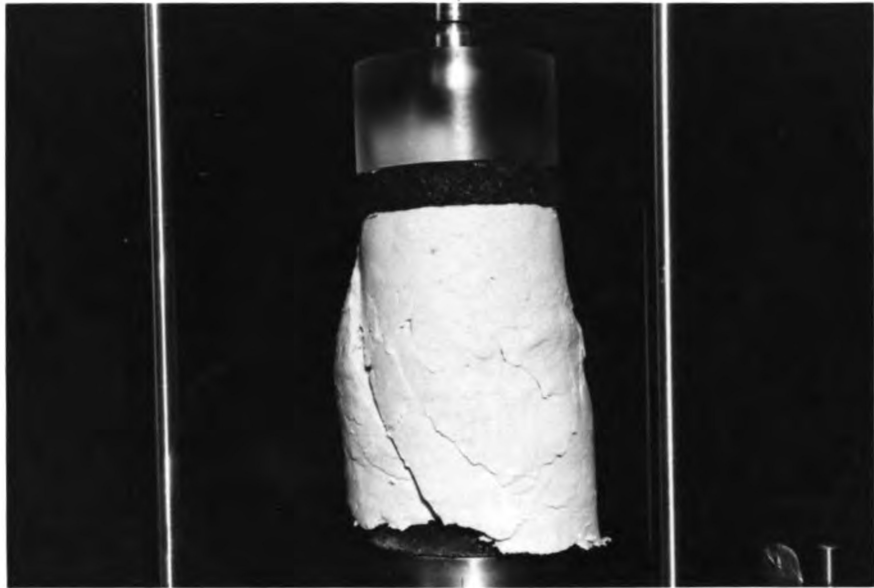


(a) W-K-U-5

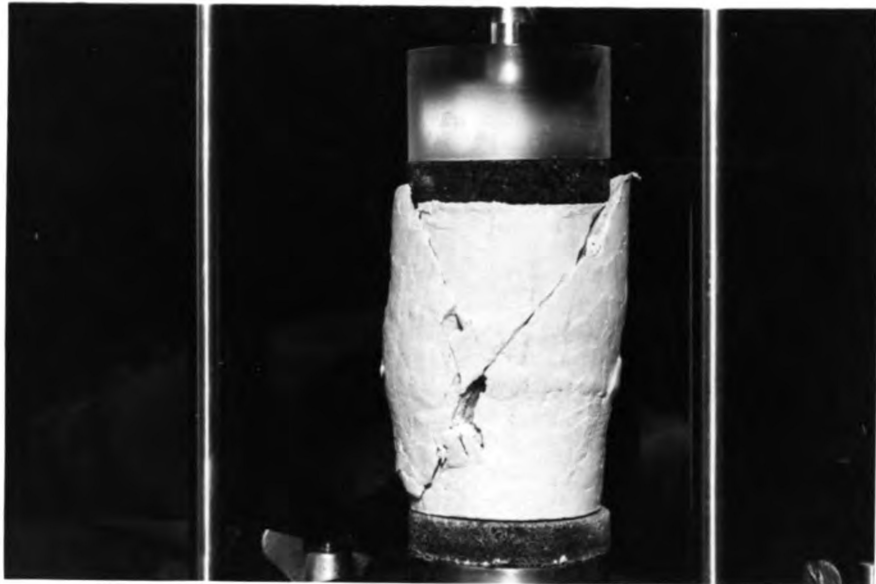


(b) W-K-U-6

Fig. 30. Photographs of deformed specimens.

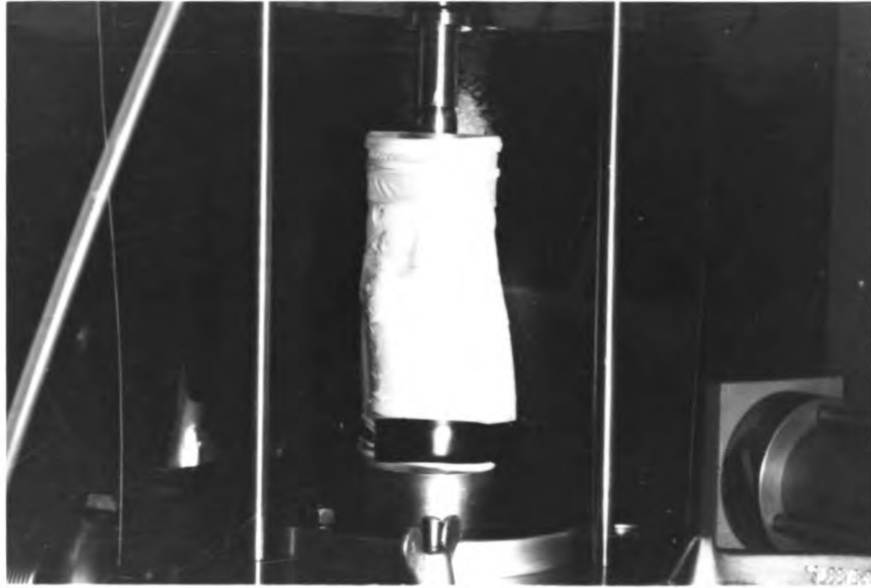


(a) W-K-U-7 (Front view)



(b) W-K-U-7 (Side view)

Fig. 31. Photographs of deformed specimens.

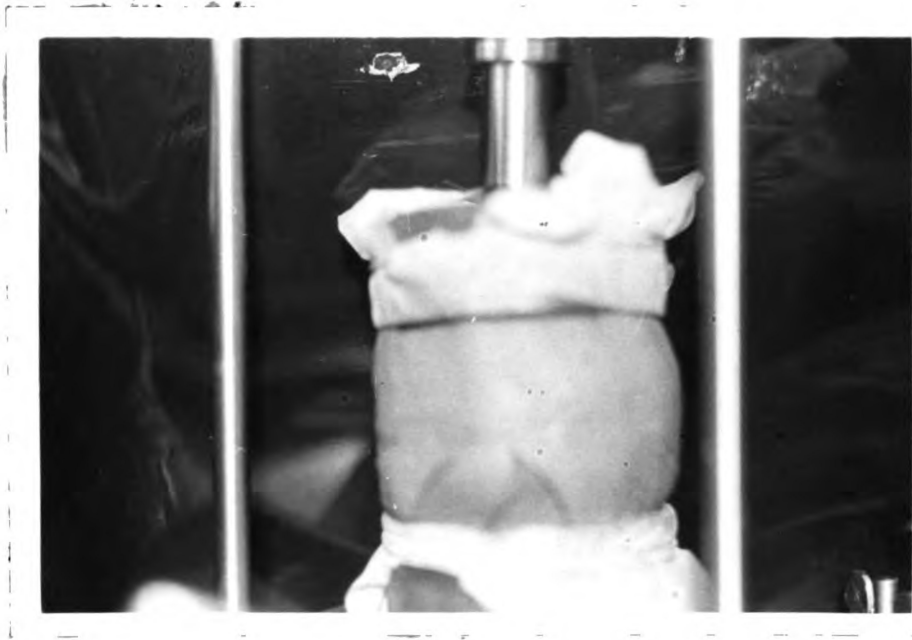


(a) W-K-U-4

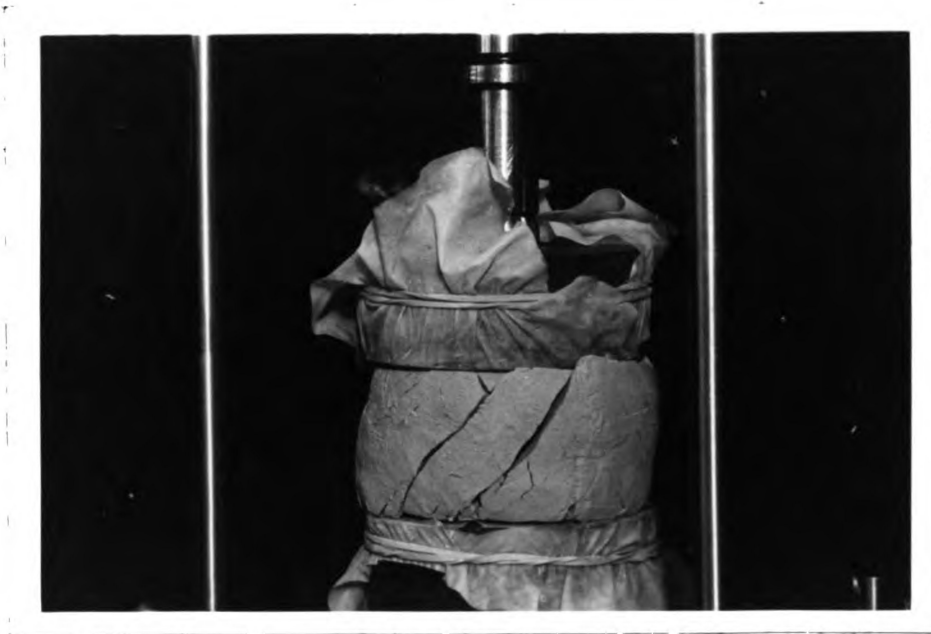


(b) W-K-U-10

Fig. 32. Photographs of deformed specimens.

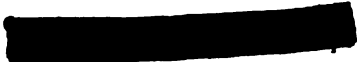


(a) W-S-U-2



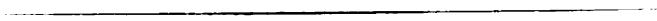
(b) W-S-U-11

Fig. 33. Photographs of deformed specimens.



ROOM USE ONLY

~~115~~ 115



MICHIGAN STATE UNIVERSITY LIBRARIES



3 1293 03178 0491